Materials Today Physics 24 (2022) 100667

Contents lists available at ScienceDirect

Materials Today Physics

journal homepage: https://www.journals.elsevier.com/materials-today-physics

# Halide perovskite based synaptic devices for neuromorphic systems

Keonwon Beom [a], Zhaoyang Fan [a, *], Dawen Li [b], Nathan Newman [c]

[a] School of Electrical, Computer and Energy Engineering, Arizona State University, Tempe, AZ, 85281, USA
[b] Department of Electrical and Computer Engineering, The University of Alabama, Tuscaloosa, AL, 35487, USA
[c] School for Engineering of Matter, Transport & Energy, Arizona State University, Tempe, AZ, 85281, USA

ARTICLE INFO

*Article history:*
Received 23 February 2022
Received in revised form
11 March 2022
Accepted 14 March 2022
Available online 23 March 2022

*Keywords:*
Halide perovskite
Memristors
Memcapacitors
Synaptic phototransistors
Neuromorphic systems

ABSTRACT

Information systems with architectures that mimic biological neural networks are of interest because they can efficiently perform adaptive learning and memory functions and process vast amount of information instantly. Halide perovskites (HPs) have been recently explored to fabricate memristors, memcapacitors, and phototransistors as neuromorphic devices used in these systems, thanks to their unique properties, which have not been seen in conventional semiconductors and metal oxides. In this review, we introduce fundamentals of artificial neural networks (ANNs), emphasize unique properties of HPs in such a context, discuss different HP-based neuromorphic devices suitable for ANNs, highlight examples on their preliminary performance demonstration, and comment on their issues and future perspectives.



## 1. Introduction

Silicon technology for massive computing is facing challenges on two frontiers: 1) the device integration density and switching speeds are approaching physical and thermal limits, and 2) the energy and time delay associated with moving data between the processors and memories limits the system performance. To meet upcoming needs of data-intensive applications, the design of future systems may need a paradigm shift to a highly distributed and massively paralleled in-memory structure [1]. Since biological nerves systems include these features and have proven to be able to efficiently process vast data rapidly, incorporating aspects of their architecture into information system design, so called neuromorphic computation, has attracted considerable interest [2].

A human brain contains ~$10^{11}$ neurons with ~$10^{15}$ synapse connections. This biological neural network (BNN) uses analog changes in neural connection strength (i.e., synaptic weight) to carry out cognition, learning, inference, and decision making with significantly higher energy efficiency (~20 W) [3] than possible with the current silicon technology. Synapse plasticity, the inelastic changes of synaptic weights, constitutes the basis of short- or long-term memory, while these changes are induced by neural spiking activities in a learning/adapting process. A neuromorphic system consists of a network of dense artificial neurons, connected by more dense artificial synapses, capable of processing information with massive parallelism and low-power dissipation. Their hardware implementation requires the extensive adoption of memory devices serving the roles of artificial synapses and/or neurons [4].

Artificial neuron-based information processing can be conducted at different neuron-mimicking levels depending on the type of neuron model used [2]. Traditional artificial neural networks (ANNs), represented by multi-layer perceptrons (MLPs) and the more advanced deep neuron networks (DNNs) [5], process data via a series of nodes (artificial neurons) interconnected by weighted links (synapses). All nodes take inputs, apply weights, sum together, then produce their outputs, similar to how biological neurons operate. However, the likeness is only superficial since they do not operate on the same spiking process of biological neurons for learning and inference. Instead, they transmit information at the end of each propagation cycle using continuous valued activations. Biological neuron inspired ANNs, as the algorithm backbones of machine learning and particularly deep learning, undergo extensive supervised off-line training using labelled big data sets before they are applied for inferring. These ANNs are still trained and implemented mainly on the Si-based von Neumann computing architecture.

Neural mimic systems most closely operate like an BNN. Spiking neural networks (SNNs) inherently use artificial neurons that

* Corresponding author.
*E-mail address:* Zhaoyang.Fan@asu.edu (Z. Fan).

https://doi.org/10.1016/j.mtphys.2022.100667
2542-5293/

respond to stimuli and trigger other neurons in pulse mode [6]. In addition to neuronal and synaptic status as in MLPs and DNNs, SNNs incorporate timing information. A spiking neuron only transmits information by firing a spike after it has crossed its threshold. The fired spike to the neighboring neurons will subsequently increase or decrease their potentials.

Neuromorphic concepts can also be applied for better sensor systems. The neuromorphic devices can emulate various biological functions at the receptor, neuron, or the system level. As an example, sensory adaptation is essential to biological neural systems. The human eye can increase its sensitivity by a factor of 10,000 to 1,000,000 as it adopts from sun-light conditions to the dark. These stimulation-induced time-dependent sensitivity changes can be efficiently mimicked by neuromorphic devices. Research in this field is being developed for intelligent prosthesis, machine-human interface, and robotics [7].

Neuromorphic information processing on hardware platforms based on artificial neural and synaptic devices has the potential to achieve low power computation, parallelism, and high operation speed, and provide a more efficient approach to implementing neural network algorithms than the traditional hardware [8–11]. They also can enhance the sensory system of robots and intelligent machines. Devices must be created to mimic the behaviors of biological neurons and synapses [12–14] with extremely low power dissipation and be capable of dense integration. It is worth noting that synapses are typically the most abundant elements in a neuromorphic system and require the most real estate on a chip. As such, development of synaptic devices with a simple structure is more urgent. In this regard, non-Si-based nonvolatile memory (NVM) techniques have attracted considerable interest [15,16]. Resistive switching random-access memory (RRAM)-represented two-terminal memristors and three-terminal memory transistors have been used to fabricate NVM-based artificial synapses. The typical synaptic devices are modulated using electrical signals, although the use of light modulation may provide new functions and capabilities. This approach may be particularly useful for systems that involve sensing.

Various materials that exhibit controllable metastable states, such as oxides [17–19], 2D transition metal dichalcogenide [20,21], and organic semiconductors [22,23], have been used to fabricate NVM devices. Halide perovskites (HPs), originally gaining widespread interest for photovoltaic and photonic applications [24–27], have also shown relevance to neuromorphic computation applications due to their desirable properties involving ion migration, defect tolerance, tunable carrier density, light-induced domain phase separation [28]. In particular, the unusual ion migration in the soft HP lattice that adversely degrades photovoltaic performance [29–31], can be advantageously exploited to produce devices that emulate biological neurons and synapses.

This work provides an overview of HP materials, including organic-inorganic hybrid and all-inorganic HPs for artificial synapses used in both DNNs and SNNs. The paper is organized as follows: Section 2 briefly introduces the basic concepts of artificial neuron-based information processing. Section 3 describes HP materials and their properties in the context of ANNs (including SNNs). Section 4 discusses different HP-based NVM devices suitable for ANNs. Section 5 presents adoption of these devices in artificial neuron systems. Finally, Section 6 highlights issues and future perspectives for HP-based synaptic devices.

## 2. Concepts of DNNs and SNNs

### 2.1. DNNs and their implementation with memristive synapses

#### 2.1.1. DNN concepts

A simplified biological neuron is shown in Fig. 1(a), mainly consisting of 1) dendrites, which couple to axon terminals of other neurons via synapses for receiving signals, 2) soma, which integrates (sums up) all received signals and fire a spike (action potential) when a threshold is surpassed, and 3) axon terminals that transmit signals to other neurons. Correspondingly, a fundamental neuron model is shown in Fig. 1(b), where the neuron acts as a processing unit. The output signal $x_i$ from a pre-synaptic neuron is coupled to this (post-)synaptic neuron via the synapse with a coupling factor (or synaptic weight) $w_i$. All these weighted inputs $w_i x_i$ ($i = 1, 2, \ldots$) are then summed up in the post-synaptic neuron, and then a non-linear transformation according to an activation function, e.g., a sigmoidal function, is performed, which produces the neuron's output signal.

A number of neurons are connected to each other, forming an ANN. The connections are generally organized into layers, with outputs of neurons in one layer providing inputs to neurons in the next layer. ANNs consist of one input layer, one output layer and one or more middle hidden layers. Those with two or more hidden layers are known as DNNs. The fully connected network, i.e., each neuron in one layer is connected to all neurons in the next layer, is usually called as multilayer perceptrons (MLP), such as the one shown in Fig. 1(c). Feed forward neural networks are fundamental, but there are many other DNN structures such as the recurrent neural network (RNN) that has loops and allows the output computed at layer 'i' at time 't' being fed back to an earlier layer at time 't+1'.

DNNs have proved to be very successful for tasks such as pattern classification and speech recognition, via extensive supervised training techniques, particularly the gradient descent algorithms and the backpropagation rule. During training, the input signal presented by each labelled sample from a training database propagates in the forward direction from the input to the output layer, passing through the multiplication by synaptic weights of each layer and the summation at the input of each hidden/output neuron. The output is compared with the target response of the network, i.e., the label on the sample, to yield an error signal (i.e., loss). This error signal is then backpropagated to the input layer to update all the synaptic weights. This process is repeated for a certain number of cycles, called as epochs, for each sample in the training database, so that all the synaptic weights are tuned to achieve the "global" most accurate outputs for this specific training database. After train and verification, a single pass of the forward propagation will produce the output when inferring.

One of the important challenges of ANN applications is how to train these neural networks effectively and quickly since it is a data-intensive process. In fact, one of the reasons for the resurgent popularity of ANNs is that they can be trained efficiently using graphic processing units or more advanced tensor processing units. It is important to remember that these processing units are still based on von Neumann platforms, and the training and inferring of DNNs are still inflicted with inherent inefficiencies.

To accelerate DNN computation and improve energy efficiency, DNN chips are being developed with the brain-inspired in-memory computing feature. Memory devices also enable the

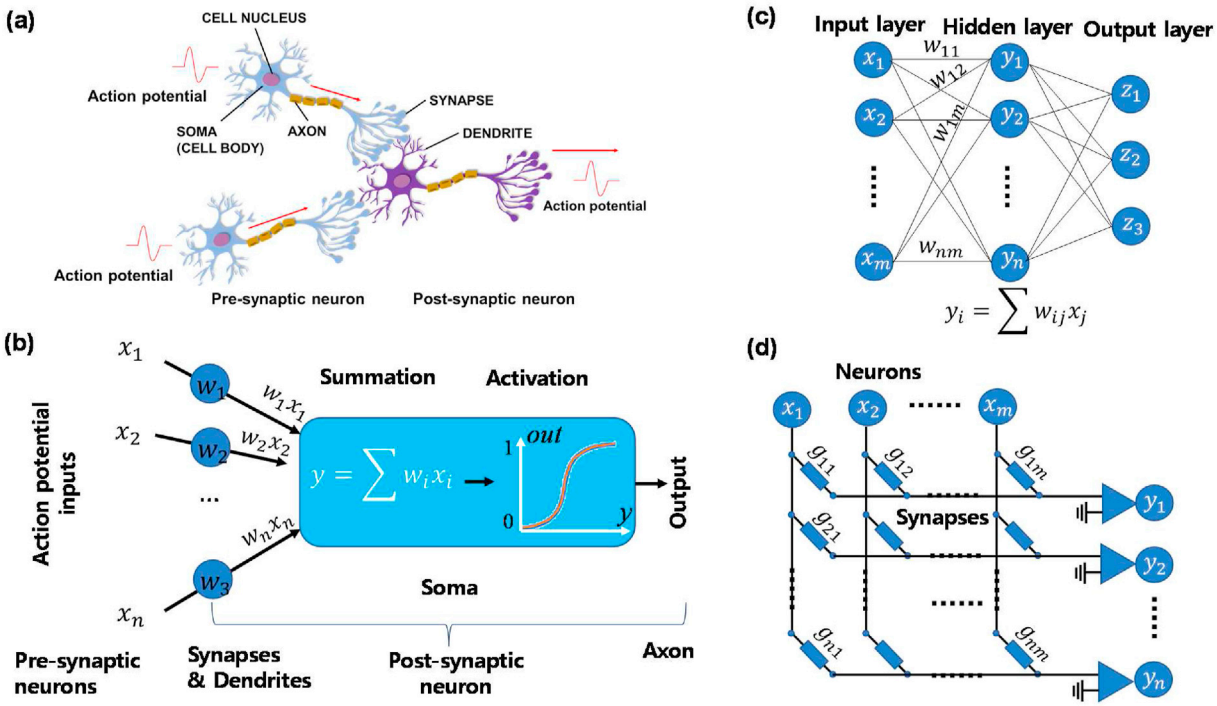


**Fig. 1.** Schematics of (a) biological neurons, (b) a fundamental neuron model, (c) a 3-layer feedforward MLP, and (d) the crossbar structure for two adjacent neuron layers to implement MVM.

implementation of learning schemes by emulating the biological synaptic plasticity. Both digital and analog memory devices are being exploited [32,33]. Crossbar memory arrays with their intrinsic matrix vector multiplication (MVM) function, have emerged as a promising approach for in-memory computing [34]. This is because the computation intensive MVM is a basic operation in all ANNs.

### 2.1.2. MVM operation and memristive synapses

In the forward propagation of an MLP, a neuron $m_i$ in a layer generates a signal $x_i$ that is sent out to all neurons $n_j$ in the next layer after being multiplied by the synaptic weight $w_{ji}$ that connects neuron $m_i$ with neuron $n_j$. The total signal $y_j$ received by neuron $n_j$ is given by the accumulation of all weighted signals from neurons in the previous layer, which thus reads $y_j = \sum_i w_{ji}x_i$, or in matrix-vector format:

$$\mathbf{Y} = \mathbf{W} \cdot \mathbf{X}$$

where $\mathbf{Y}$ is the vector of $y_j$, $\mathbf{W}$ is the matrix of $w_{ji}$, and $\mathbf{X}$ is the vector of $x_i$.

The crossbar architecture of a programmable resistance network has its intrinsic MVM function based on two physical laws: Ohm's law of $i_{ji} = g_{ji}v_i$ and Kirchhoff's current law of $i_j = \sum_i i_{ji}$, where $g_{ji}$ is the conductance. This architecture is illustrated in Fig. 1(d), where two adjacent layers of neurons are connected by a resistance network in a crossbar format, with the pre-synaptic layer of neurons identified by the column number $i$ and the post-synaptic layer of neurons by the row number $j$. The synaptic weight $w_{ji}$ is represented by the conductance $g_{ji}$ of the programmable resistance that connects column $i$ to row $j$. Then the physical laws determine:

$$\mathbf{I} = \mathbf{G} \cdot \mathbf{V}$$

Thus, the analog MVM is executed instantaneously in parallel. After a nonlinear transformation according to an activation function by post-synaptic neuron layer, voltage signals, converted from currents, will be delivered to the next neural layer.

It is obvious that in such a structure, the number of artificial synapses (N x M) is much larger than the number of artificial neurons (N + M). The small number of neurons can be implemented by specific artificial neuron devices, peripheral Si circuits, or even software, while the synapse ideally should be implemented by a simple conductance-tunable device for high integration density [35]. To meet accuracy, such a programmable conductance-based synapse should have a wide dynamic range with quasi-continuous or multilevel states (>~100) and linear tunability under programming pulses [34], crucial for analog computation.

In this regard, some of the emerging non-Si NVMs could be strong candidates for creating artificial synapses to conduct in-memory computation. This is particularly true for RRAM that can modulate its resistance in an analog way with multilevel operation via the storage of several bits, as well as high scalability up to 10 nm in size and the opportunity to achieve 3D integration.

## 2.2. SNNs and their implementation with memristive synapses

### 2.2.1. SNN concepts

In comparison to DNNs, SNN networks are more directly inspired by the human brain. They promise to bridge the gap between ANNs and BNNs by exploiting biologically plausible neurons that offer unsupervised learning, faster inference, lower energy expenditure, and event-driven information processing capabilities. While their effectiveness has been described theoretically and proved in preliminary demonstrations, SNNs have not yet been widely used in real life applications. Generally, platforms based on the spiking neuron model is classified as neuromorphic architectures—otherwise known as biologically inspired computing architectures.

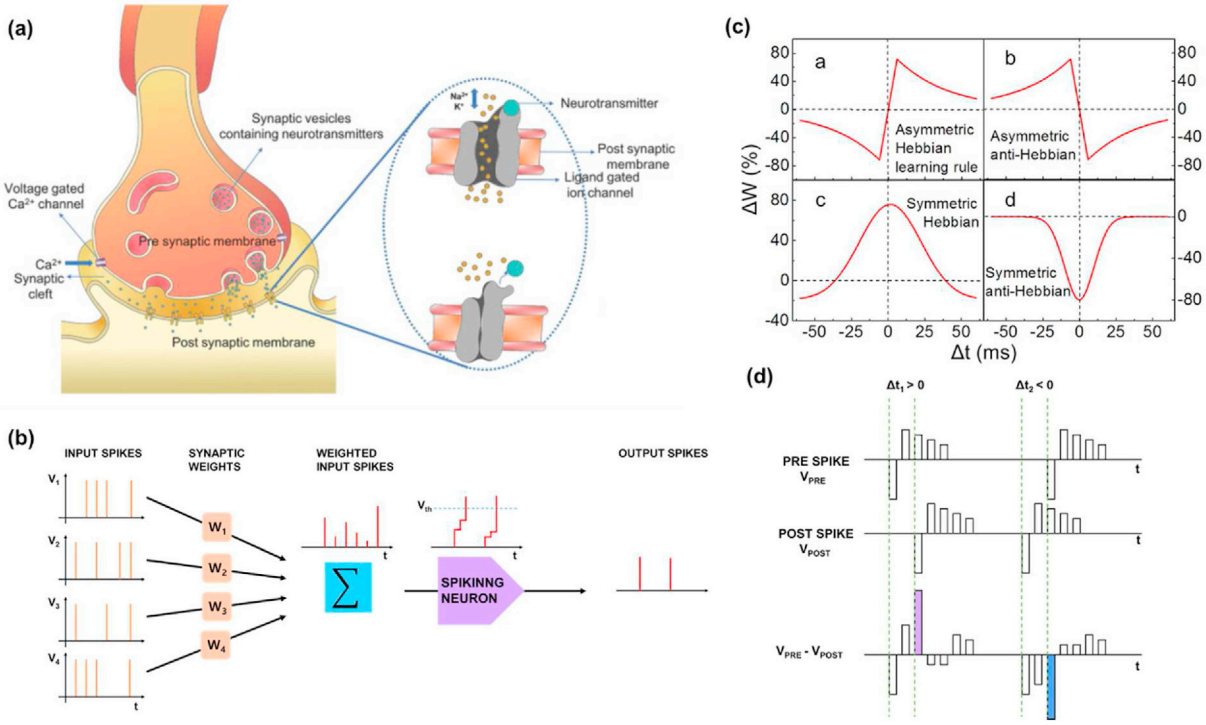


**Fig. 2.** (a) Schematic of chemical synaptic transmission. Arrival of an action potential causes selective endocytosis and exocytosis of $Na^+$, $K^+$, and $Ca^{2+}$ deciding the extent of membrane polarization. Reproduced with permission [37]. Copyright 2018, Wiley-VCH. (b) Schematic of SNNs. (c) Ideal STDP learning rules. Reproduced with permission [39], Copyright 2014, Springer Nature. (d) The scheme of voltage pulse overlapping at the device terminals for STDP demonstration.

In BNNs, a synapse is the functional link transferring the chemical signals between two consecutive neurons, as shown in Fig. 2(a) [36,37]. Neurotransmitters released from the presynaptic neurons react with receptors on the postsynaptic membrane to change the membrane potential, resulting in an excitatory postsynaptic potential or an inhibitory postsynaptic potential within a few milliseconds timescale [38]. If the accumulated potential in the post neuron is over a threshold, an action potential is fired and transferred further to other neurons. Otherwise, the accumulated potential will recede back to its resting value due to ionic leakage. The rate of spike generation and the temporal pattern of the spike train contain information of external stimuli and ongoing calculations. The sparsity of communication spikes results in high energy efficiency of brain activities.

An SNN architecture, consisting of spiking neurons and weight-adaptable synapses, captures the spiking feature of the BNN with energy efficiency (Fig. 2(b)). The analog inputs are encoded into the spike trains using rate, temporal, or population coding. In contrast to BNNs that have both action potential dynamics and network dynamics, highly simplified dynamics are adopted in SNNs. For example, the original Hodgkin and Huxley model contains extensive biological details and has high computational cost, so many simplified neuron models are more commonly used, with the leaky integrated-and-fire (LIF) neuron extremely popular because it captures the intuitive properties of external input accumulating charges across a leaky cell membrane with a clear threshold.

### 2.2.2. Unsupervised learning in SNNs

Neurons are linked through synapses, which can be excitatory or inhibitory. The synaptic weight has the behavior of locally associative synapse strengthening and weakening, implemented by long-term potentiation (LTP) and depression (LTD). Spike timing, firing rate, synaptic cooperativity, depolarization, and others, all govern plasticity induction in BNNs, and the relative importance of these factors varies across synapses and activity regimes [40]. Since the associative synapse plasticity is considered as the basis of learning and memory in BNNs, the corresponding bio-plausible associative learning rules that cannot be replicated in DNNs, but enabled by artificial spiking neurons, have been proposed for unsupervised learning, including spike-timing-dependent plasticity (STDP), spike-rate-dependent plasticity (SRDP), and others.

In the STDP-based Hebbian learning and its many variants, the order and precise temporal interval between presynaptic and postsynaptic spikes determine the sign and magnitude of LTP or LTD. The temporally and spatially local synaptic weight change $\Delta w$ is correlated to the relative spiking times between the pre- and post-synapses, $\Delta t = t_{post} - t_{pre}$ (~ tens of $ms$), via Eq. (1):

$$\Delta w = \begin{cases} Ae^{\Delta t/\tau}, & A>0 \text{ for } \Delta t>0 \\ Be^{-\Delta t/\tau}, & B<0 \text{ for } \Delta t<0 \end{cases} \quad (1)$$

This equation has an intuitive interpretation that if the pre- and post-synaptic events have a causal relationship ($\Delta t > 0$), $w$ is strengthened; otherwise, it is weakened.

STDP can be found in various shapes and forms depending on the stimulating spike or the type of synapse. As shown in Fig. 2(c), the polarity of synaptic weight change can be determined by the temporal order of the pre- and post-synaptic spikes. In other cases, it is only determined by the relative timing of the pre- and post-synaptic spikes, and this dependency results in symmetric Hebbian or symmetric *anti*-Hebbian learning rule [39,41]. Besides the temporally and spatially local weight change, it deserves to be emphasized that STDP also has important temporally accumulated network-level effects, which has not been well exploited.

In contrast to spike timing in STDP, in SRDP-based learning, it is the rate of spikes emitted by externally stimulated neurons that determines the synapse potentiation or depression, with high

frequency stimulation leading to synaptic potentiation and vice versa [42]. Intensive efforts have been made for hardware implementation of brain inspired SNNs based on STDP and SRDP [43,44].

Synaptic weights can also be changed in other processes. Synaptic plasticity is classified as short-term potentiation/depression (STP/STD), with synaptic weights temporarily changed for milliseconds to a few minutes, or LTP/LTD that can be maintained much longer. Paired-pulse facilitation/depression (PPF/PPD) is a common synaptic function in STP, for which, consecutive pre-synaptic spikes can either increase or decrease the concentration of calcium ions in the pre-synaptic neuron, causing amplified or attenuated change in post-synaptic potential. LTP is induced by repeated and/or strong pre-synaptic spikes. STP/STD can be transformed to LTP/LTD by controlling the rate and/or intensity of the spikes generated from the pre-synaptic neurons [16].

#### 2.2.3. STDP implementation with memristive synapses

The earliest STDP demonstration at the memrisitive level was performed based on a scheme of voltage pulse overlap at the device terminals, with the pre-spike voltage minus the post-spike voltage as the voltage on the synaptic device [45]. As shown in Fig. 2(d), the spike consists of a series of single pulses in consecutive timeslots, starting with a negative pulse which is followed by positive pulses with decreasing amplitude. The pulse amplitudes are limited to a value so that no single pulse can affect the device resistance. Only when there is an overlap between the pre-spike and the post-spike pulses a programming pulse can be generated for which the amplitude is large enough to modulate the resistance. Thus, the first negative pulse acts as an enable function to determine which positive pulse could contribute to the programming pulse. For smaller $|\Delta t|$, the negative pulse overlaps a positive pulse with larger amplitude (the red or blue one in the figure), leading to a larger conductance change. If $\Delta t$ is positive, the conductance increases, while for a negative $\Delta t$, it decreases. This scheme implements the asymmetric Hebbian learning rule. However, using a single RRAM device as the spike synapse suffers from issues such as current control requirement, sneak paths in a crossbar array, and a high-power consumption.

A hybrid CMOS/memristive STDP synapse using the 1T1R structure can solve these problems [46]. The scheme also uses the voltage pulse overlap to implement potentiation/depression at positive/negative $\Delta t$ between the pre- and post-spikes. The achieved STDP characteristics, due to the RRAM device operation in the binary mode, displays a square profile, in contrast to the exponentially decaying behavior exhibited by biological synapses. Even so, such one-transistor-one-resistor (1T1R) synapses have been incorporated in many SNNs for neuromorphic tasks such as unsupervised learning of spatiotemporal auditory/visual patterns and associative memory.

The pulse overlap scheme suffers from the high-power consumption caused by the extended pulse duration that must be long enough to allow the conductance change occurring. A long pulse duration also slows the processing frequency, leading to low throughput in large SNN systems. Therefore, other memristive concepts that allow bio-realistic synaptic plasticity using non-overlap schemes are attracting increased interest. One example is to leverage the resistive switching in second order memristors that have short-term memory effects in the time evolution of second-order variables, which could be the internal temperature, atomic metal bridge, or others [47]. By sequential application of two spikes with a certain $\Delta t$, the short-term memory effect will result in STDP behavior. Another attractive design is the one-selector-one-resistor (1S1R) structure, in which a volatile resistive switching device (or diffusive memristors) as the selective device is in series with a RRAM that serves as the resistor [48].

Interestingly, these devices used in the non-overlap scheme for STDP implementation, with their short memory function, are also capable of capturing SRDP potentiation and depression function depending on the spiking rate of the applied pre- and post-spikes. Their applications in neuromorphic systems have also been investigated in simulation and hardware demonstration.

This short summary suggests that memory elements with programmable conductance, such as memristors and memory transistors, have great potential in the implementation of both DNNs and SNNs, providing a wide portfolio of functionalities, such as non-volatile weight storage, in-memory computing and parallel computing via MVM, online weight adaptation in response to external stimuli, high integration density and scalability, and energy efficiency [16].

In the following sections, we will review halide perovskites-based memristive devices and their applications in neuromorphic computation. But before that, the relevant material properties that could be exploited for synaptic device designs are highlighted.

## 3. Relevant halide perovskite properties

### 3.1. Crystal structure, composition, and tunable bandgap

HPs have an $ABX_3$ perovskite structure consisting of monovalent A-site cations (such as organic $MA^+$=$(CH_3NH_3)^+$ and $FA^+$=$(CH(NH_2)^{2+}$ and inorganic $Cs^+$), divalent B-site metal cations ($Pb^{2+}$, $Sn^{2+}$, $Cu^{2+}$) and X-site halide anions ($Cl^-$, $Br^-$, $I^-$). As shown in Fig. 3(a), the corner-sharing $[BX_6]^{4-}$ octahedra are arranged in a cubic form, with monovalent A-site cations occupying the cuboctahedral cavities in the B-X sublattice [49]. Here, the A-site cation must be small enough to fit within space of the octahedral to maintain the structure integrity. Tolerance factor empirically is determined by the Goldschmidt rule, which limits the radius of the A cation in the range of 0.8−1.2 for most 3-D perovskites [50,51]. A few organic molecular ions such as $MA^+$ and $FA^+$, as well as inorganic $Cs^+$ are suitable for the steable 3-D metal-halide perovskite lattice.

In addition to the 3D perovskite lattice, lower-dimensional HPs, from 0-D $BX_6$ to 2-D perovskite, also exist. 2-D perovskites consist of single (or multiple) inorganic sheets sandwiched between organic layers held together by Coulombic forces [55,56]. As shown in Fig. 3(b), the pure 2-D perovskite ($n = 1$) typically has a $R_2BX_4$ formula where R is a bulky organic cation that acts as a spacer between the inorganic sheets [52]. For $n > 1$, quasi-2D perovskite can be obtained when a small organic cation(A) such as $MA^+$ combines with organic cation, resulting in the formation of multi-layered $R_2A_{n-1}B_nX_{3n+1}$ which converges into the bulk 3-D structure at $n = \infty$. This structure can extend the limit on the cation dimension determined by the Goldschmidt tolerance factor, providing structural flexibility for several organic cations.

The flexible dimensionality of HPs can be utilized to tune their bandgap through a quantum confinement effect at reduced dimensionality. As an example, the $(BA)_2(MA)_{n-1}PbI_{3n+1}$ structure was synthesized with $n = 1, 2, 3, 4$ and $\infty$, which exhibits decreased bandgap from 2.24 eV ($n = 1$) to 1.52 eV ($n = \infty$) [55]. In this structure, the small $MA^+$ cation is replaced by a much larger organic $BA^+$ cation, resulting in the 2-D perovskite via steric effects and forming multiple-quantum well structures in which inorganic Pb layers act as “wells” and organic layers act as “barriers”. The narrower the width of the inorganic layers, the smaller the dispersion of the bands, resulting in wider bandgap. Bandgap tuning by adjusting the ratio of methylammonium (MA) in $(C_6H_{13}NH_3)_2(CH_3NH_3)_{m-1}Pb_mI3_{m+1}$ was also demonstrated with the bandgap changed from 1.7eV ($n = \infty$) to 2.7eV ($n = 1$, monolayer) [57].

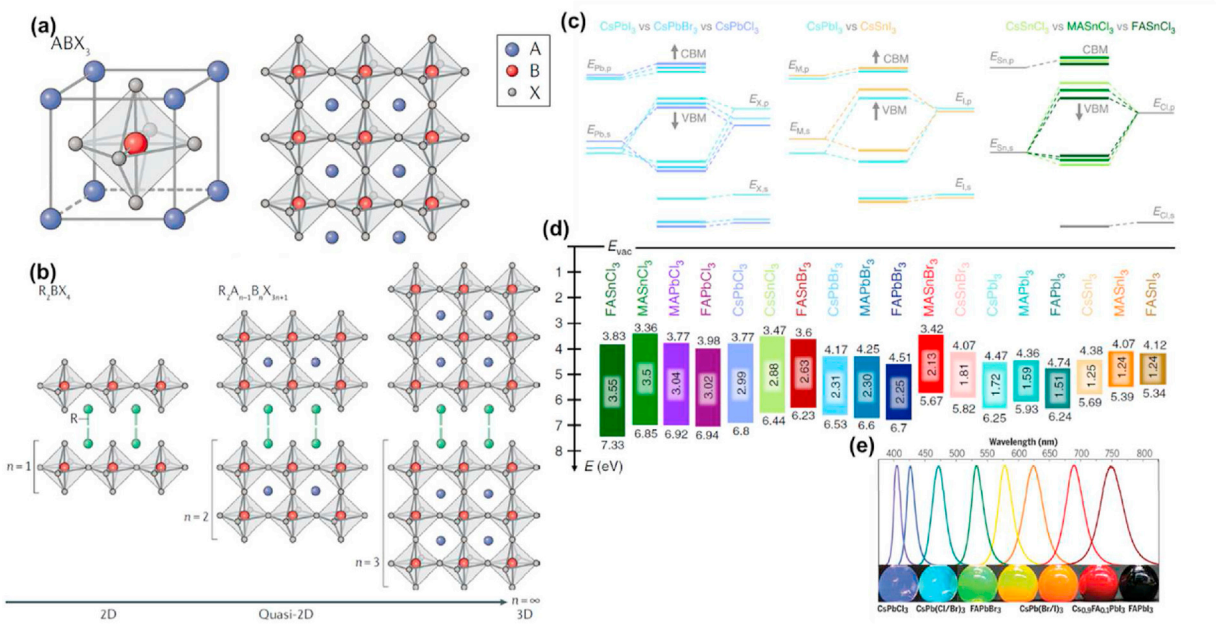


**Fig. 3.** (a) Illustration of the 3D $ABX_3$ perovskite structure, showing the corner-sharing $[BX_6]^{4-}$ octahedra where A is an organic or inorganic cation, B is a metal cation, and X is a halide anion. (b) Illustration of the structures of low-dimensional perovskites with different numbers of $[BX_6]^{4-}$ layers ($n$). Reproduced with Permission [52]. Copyright 2019, Nature Publishing Group. (c) Schematic of energy levels in $ABX_3$ HPs with variation of halide anions and metal cations. (d) Schematic energy band diagram of the typical 18 metal halide perovskites. Reproduced with Permission [53]. Copyright 2019, Springer Nature. (e) PL spectra and corresponding images of composition tuned A (Pb)$X_3$ nanoparticles. Reproduced with Permission [54]. Copyright 2017, AAAS.

HP based synaptic devices with dimensionality dependent properties was studied [58]. Kim et al. demonstrated memristive artificial synapses based on $(PEA)_2MA_{n-1}Pb_nBr_{3n+1}$ with the MA ion replaced by a bulky PEA ion. As $n$ increased, photoluminescence (PL) became yellowish, suggesting a shift toward larger bandgap [55,58]. Furthermore, in the quasi-2D perovskites, the larger insulating PEA cations hinder charge transport and result in a decrease of conductivity as $n$ decreases. This effect causes the variation observed in their paired-pulse facilitation (PPF), energy consumption, and memory retention.

In additional to relying on the structural dimensionality, the bandgap of HPs can also be tuned by substituting cations and halides with different ones or changing the cation ratio if mixed cations are used. In general, the valence band maximum (VBM) of HPs is composed of the hybridization of the metal cation *s* orbital bonding state and the halide *p* orbital anti-bonding state, whereas their conduction band minimum (CBM) is determined mostly by the metal cation *p* bonding state and the halide *s* anti-bonding state. A-site cation does not participate in covalent bonding, but only influence the electronic structure indirectly through the lattice space variation [53].

Fig. 3(c) shows the effect of varying A, B or X ions on their CBM and VBM. For instance, the CBM in the $CsPbX_3$ structure is mainly determined by the position of the Pb *p* orbital level, but it increases as the larger I substituted by the smaller Br and Cl atoms. Density-functional-theory (DFT) determined energy band diagrams of various HPs are shown in Fig. 3(d). The tunability of their optical bandgap, by exchanging or mixing different A, B, and/or X ions, was demonstrated in Fig. 3(e). These changes are well characterized for many primary $ABX_3$ structure as well as well as more complex perovskite structures in experimental [59–61] and computational studies [62,63]. The optical bandgap changes with the cation ratio [64] and the halide ratio [54,65–67] are well documented.

Various crystal structures, composition and tunable bandgaps of this HP material system offer many options and possibilities for synaptic device design tailored for particular applications in DNNs, SNNs, and sensory.

### 3.2. Dense vacancies and their doping effect

HPs have higher defect tolerance [53,68–70] and lower point defect formation energies [71] compared to strongly bonded semiconductors. They can maintain their crystal structures even with a high density of point defects. Although vacancies generally should be avoided for device stability, dense vacancy generation in HPs could be exploited for better use in neuromorphic devices.

Fig. 4(a) shows the energy levels of various neutral and charged vacancies ($V_{Pb}$, $V_{MA}$, $V_I$), interstitials ($Pb_i$, $MA_i$, $I_i$) and antisites ($Pb_I$, $I_{Pb}$) in $MAPbI_3$. Although the reported formation energies from different authors show qualitative differences [70–73], vacancies have energy levels lying near or within the CB or VB and they have low formation energies. In contrast, energy levels of most interstitial and anti-site defects such as $I_{Pb}$, $I_{MA}$, $Pb_i$, and $Pb_I$ are located within the gap, and most form deep traps with formation energy higher than those of vacancies [72].

Due to their small formation energy, elemental defects such as $V_{Pb}$, $V_I$, $V_{MA}$ are common in HPs, and they act as unintentional dopants [74–77]. A significant amount of self-dopants were discovered in $MAPbI_3$ that produced either *n*- or *p*-type conductivity, depending on the ratio of MAI and $PbI_2$ precursors as well as post-growth annealing control [74]. When the $PbI_2$/MAI precursor ratio is varied from 0.3 to 1.7, the conductivity of the synthesized $MAPbI_3$ film converts from *p*-type (0.3) to *n*-type (0.65–1.7), as shown in Fig. 4(b). Furthermore, the *p*-type film, synthesized with the 0.3 ratio, can be converted to *n*-type material by reducing the MAI content in the film using thermal annealing. This is possible because $MAPbI_3$ is thermally unstable at temperatures above 150 °C [78,79]. A tunable carrier concentration and conductivity type occur due to the formed native defects that depend almost entirely on the HPs' composition. The 0.3 Pb:I ratio generates dense Pb

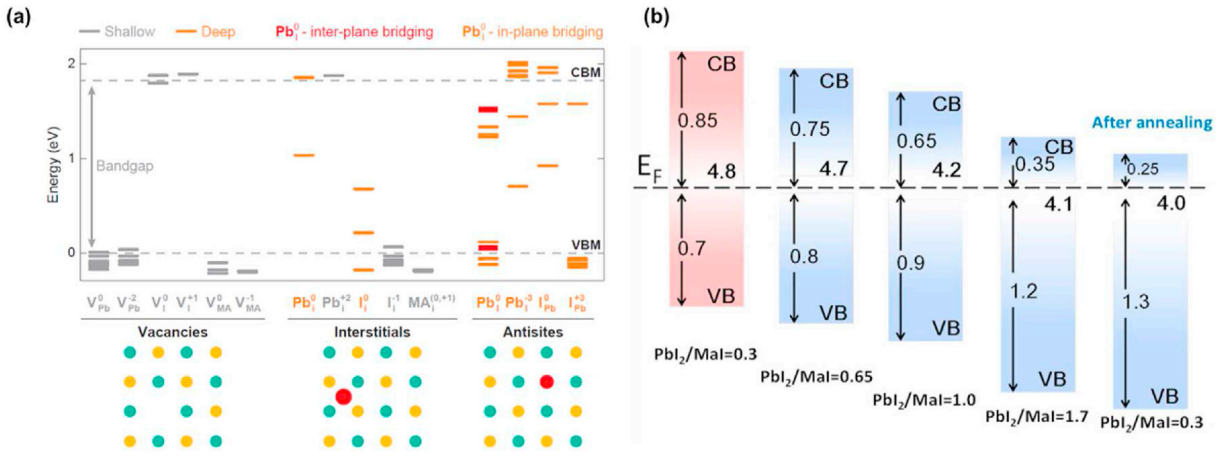


**Fig. 4.** (a) Energy levels related with the point defects corresponding vacancies ($V_{Pb}$, $V_I$, $V_{MA}$), interstitials ($Pb_i$, $I_i$, $MA_i$), and anti-sites ($Pb_I$, $I_{Pb}$). Reproduced with Permission [70]. Copyright 2014, American Chemical Society. (b) Facile tunable majority carrier in $MAPbI_3$ confirmed by ultraviolet photoelectron spectroscopy (UPS) for HP thin films with different precursor ratios of 0.3, 0.65, 1.0, and 1,7. Reproduced with Permission [74]. Copyright 2014, AIP Publishing.

vacancies, leading to *p*-type material. For a ratio of 0.65 and above, it is $V_{Pb}$ that contribute to the *n*-type conductivity. In contrast, $MAPbBr_3$ shows unipolar self-doping phenomenon [75]. This material exhibits only *p*-type conductivity as a result of the $MA_i$ donor's larger formation energy than the acceptor $V_{Pb}$.

The device engineer can choose materials with the desired conductivity, the type of carrier, and the size of the bandgap. This allows for the design of devices with controllable synaptic functions through stimulus tuned resistance changes, which are kinetically stable with a memory effect [80].

### 3.3. Ion migration

Ion migration phenomenon in oxides and other perovskites is well known [81–85]. With the increased interest in HP photovoltaics, the performance degradation from ion migration in HP solar cells has attracted great attention [86]. Ion migration has been linked to such effects as the anomalous photocurrent hysteresis phenomenon [87,88], giant capacitance [89,90], and self-doping [74,91]. A significant amount of research has focused on developing methods to suppress the ion migrations and its adverse effects. On the other hand, this same ion migration phenomenon could also be exploited for designing better ionic neuromorphic devices since the rate of ion and charged-defect migration can be controlled by external stimuli such as electrical fields and optical illuminations. To this end, it is necessary to understand the ion migration mechanism in HPs [92].

Given the small point defect formation energy in HPs, charged defects and ions such as $MA^+$, $FA^+$, $Br^-$, $I^-$ may have low barriers to migrate in the lattice. Other mobile defects such as $H^+$, which can be introduced by material decomposition or contamination, could also contribute to ion migration [93]. The activation energy ($E_A$) for a point defect to migrate in a lattice is influenced by various factors including lattice structure, ionic radius, ion-jumping distance, and the ion charge, etc. [31,94–97]. Eames et al. calculated the ion activation energies in cubic $MAPbI_3$ and proposed three different types of vacancy hopping mechanisms occurring between neighboring atoms (Fig. 5(a)): (1) $I^-$ migration along an octahedron edge (path A), (2) $Pb^{2+}$ migration along the cubic <110> diagonal direction (path B), and (3) $MA^+$ migration into neighboring vacant A-site position (path C) [94]. Their results indicate that the $I^-$ ion has the lowest activation energy (0.58 eV), followed by $MA^+$ ion (0.84 eV) and $Pb^{2+}$ ion (2.31 eV). Experimentally, an $E_A$ of 0.6–0.68 eV was inferred from photocurrent relaxation results, which falls very close to the above predictions. It is reasonable to speculate that $I^-$ ion is the most likely mobile ion in cubic $MAPbI_3$. Others also reported that $I^-$ ions have an $E_A$ of 0.08 eV and are the most mobile ion [95].

Activation energies for $FA^+$, $MA^+$, and $I^-$ in the tetragonal $MAPbI_3$ and trigonal $FAPbI_3$ cells along different migration paths were calculated [96]. The results clearly show that $I^-$ anions in both $MAPbI_3$ and $FAPbI_3$ can easily diffuse with low barriers of ca. 0.45 eV. $MA^+$ cations and larger $FA^+$ cations both have rather low barriers as well, indicating that they can migrate in HPs when a bias voltage is applied. High-charged ion, $Pb^{2+}$, is believed to have high activation energy and can be excluded from ion migration.

Substitutional defect migration always involves vacancy-related processes. Fig. 6 illustrates possible defects-mediated ion migration pathways [92]. Among them, Schottky and Frenkel defects are most often the dominant migrating species, which are readily created in HPs, particularly if synthesized in a conventional solution process. Their typical density falls in the range of $10^{15}$ to $10^{18}$ $cm^{-3}$ [98–101]. The formation energy of $MAPbI_3$ from MAI and $PbI_2$ is 0.11–0.14 eV, suggesting their soft matter nature [101]. This energy is close to the average thermal energy of 0.093 eV estimated for 85 °C (assuming six degrees of freedom). Since $MAPbI_3$ synthesis involves an annealing step at this or even higher temperature, instability of individual unit cells at such a temperature will result in their decomposition with time. It is their rather low formation energy that causes the mechanical softness and significant dynamical and static structural disorder in $MAPbI_3$-represented halide perovskites.

With their typical sub-micron scale crystalline size, polycrystalline HP films contain a dense network of GBs (Fig. 6(c)). Because of the structural disorder and significant strain fields near them, GBs affect ionic migration in HPs, although whether they facilitate or hinder the migration of specific ionic species has not been established yet [102–107]. In general, the activation energy for ion migration is typically much smaller along these extended defects [106]. The structural disorder and strain fields often attract a significant concentration of native and impurity defects, resulting in defect gettering and segregation [103,105,108]. Their presence is often referred to as Cottrell clouds.

It is difficult to pin down which channel is the dominant pathway for ion migration in polycrystalline films, due to a huge Schottky defect density in the grain and a larger cross-section area

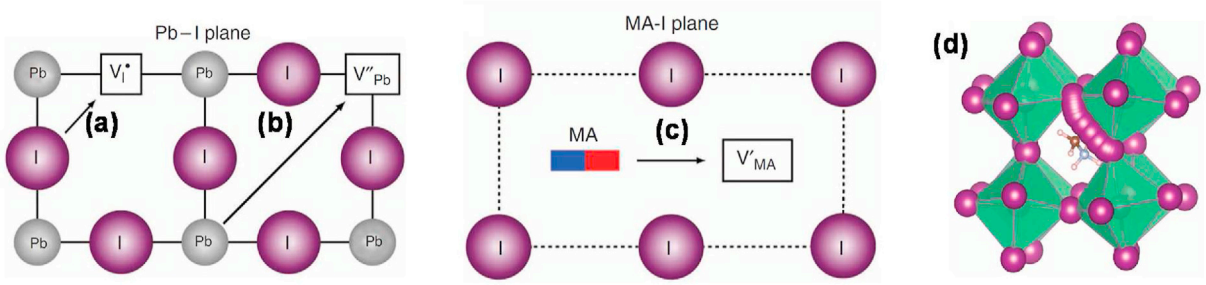


**Fig. 5.** Schematic illustration of ion migration pathways for (a) $I^-$ anion and (b) $Pb^{2+}$ cation in the Pb–I plane, and (c) $MA^+$ cation in the MA-I plane. (d) Migration path of I- ions along the $I^-$ $I^-$ edge of $PbI_6^{4-}$ octahedron in the $MAPbI_3$ structure calculated from density functional theory (DFT). Reproduced with Permission [94]. Copyright 2015, Nature Publishing Group.

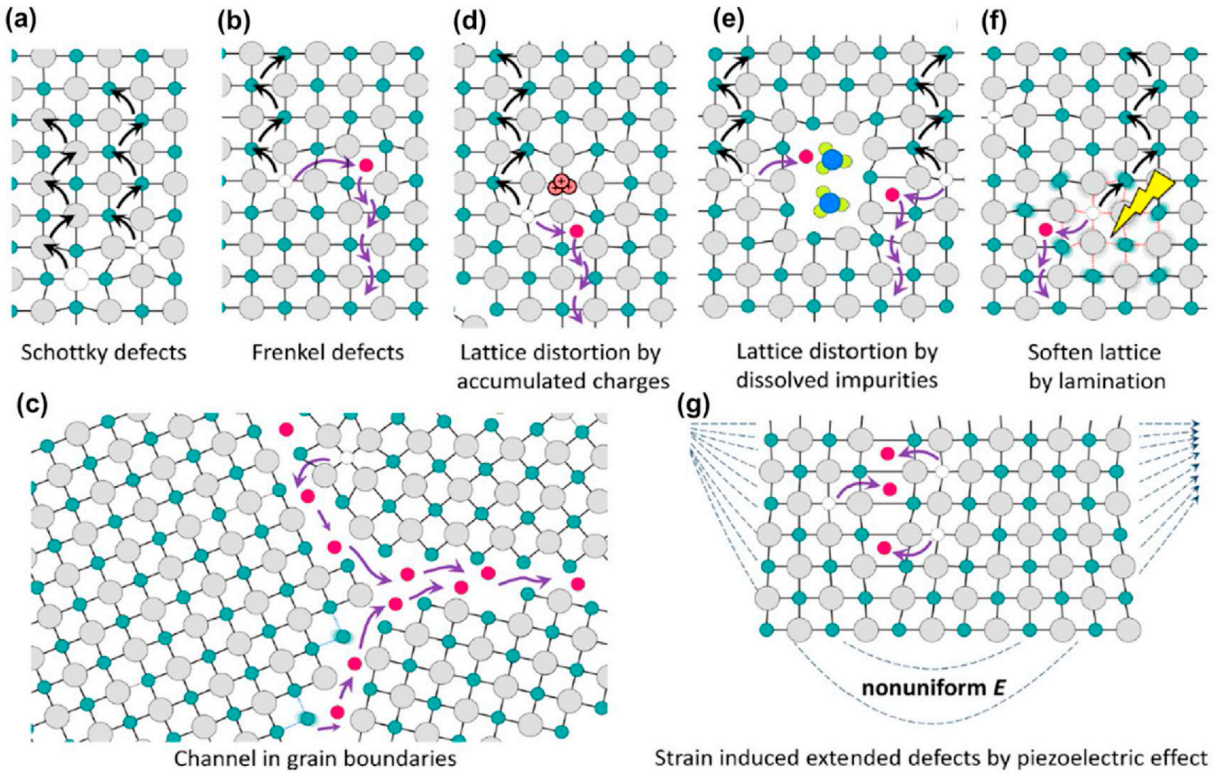


**Fig. 6.** Illustration of the ion migration pathways enabled by (a) Schottky defects, (b) Frenkel defects, (c) open space and wrong bonds at grain boundaries, (d)–(f) lattice distortions due to accumulated charges (d), dissolved impurities (e), and nonuniform strain caused by piezoelectric effect (f), and (g) soften lattice caused by the light illumination induced bond weakening. Reproduced with Permission [92]. Copyright 2016, American Chemical Society.

for bulk ion migration. In addition to Schottky and Frenkel defects and GBs, soften lattice (Fig. 6(f)) [109] and lattice distortion (Fig. 6(d) and (e)) [110] provide other possible pathways for ion migration.

Considering the crucial roles played by ion transportation in biological neurons, the ionic migration property in HPs significantly enhances the weight of this material system as a candidate, which deserves to be well exploited for designing better neuromorphic devices.

### 3.4. Modulating the interface charge density via ion migration with applied electric field

The charge carrier density in HPs can be tuned by controllably adjusting the alloy composition during material synthesis, as described earlier. However, a potentially more effective method is to modulate the carrier density *in-situ* using external stimuli to induce ion migration. With the density of mobile ions modulated at the interface between the perovskite and its electrode, electron concentration will also correspondingly be changed [111–114].

For the switchable photovoltaic effect observed in an Au/$MAPbI_3$/PEDOT:PSS structure, an applied electric field induces the drift of charged $V_I$, $V_{Pb}$ and/or $V_{MA}$ at the two electrode/perovskite interfaces, where negatively charged $V_I$ acts as a donor while positively charged $V_{Pb}$ and $V_{MA}$ act as acceptors [113]. Ion aggregation results in the formation of an *p-i-n* structure during the positive pooling process, which can be transformed to an *n-i-p* structure by ions drift when applying the opposite voltage polarity (Fig. 7 (a) and (b)). The change in structure was verified by monitoring the large shift in the work-function using Kelvin probe force microscopy. The redistribution of $MA^+$ ions was also observed in the $MAPbI_3$-based lateral structure and two types of ions

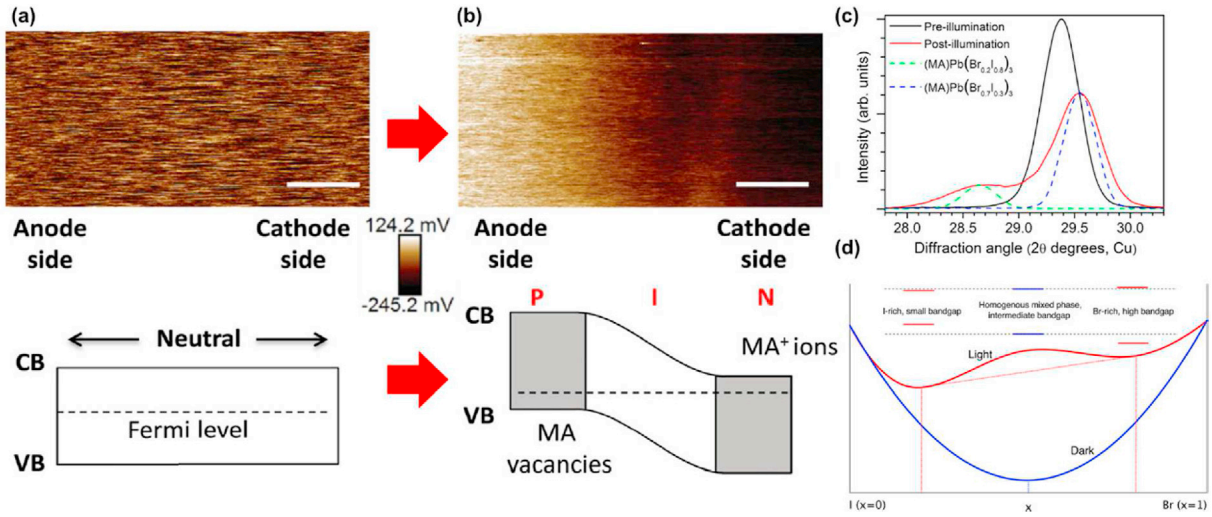


**Fig. 7.** KPFM potential images and energy diagram of $MAPbI_3$ thin film between the two Au electrode before (a) and after (b) fields applied. Reproduced with Permission [113]. Copyright 2015, Wiley-VCH. (c) The (200) XRD peak of $MAPb(Br_xI_{1-x})_3$ film with $x = 0.6$ before (black) and after (red) white-light soaking. XRD patterns of an $x = 0.2$ film (dashed green) and an $x = 0.7$ film (dashed blue) are included for comparison. Reproduced from Ref. [115] with permission from The Royal Society of Chemistry. (d) Schematic Helmholtz free-energy curves of $MAPb(Br_xI_{1-x})_3$ mixed-halide in the light and in the dark. Reproduced with Permission [116]. Copyright © 2016 American Chemical Society. (For interpretation of the references to colour in this figure legend, the reader is referred to the Web version of this article.)

contributing the ionic conductivity were identified: "fast-ions" that dominate the migration at a smaller electric field (0.3 V/μm) and "slow-ions" that require a higher electric field (3 V/μm) [113]. This field-dependent ion drift mechanism can be used to controllably adjust the synaptic weight for spike-timing-dependent plasticity (STDP) or spike-rate-dependent plasticity (SRDP).

The ability to adjust both the bandgap and the doping levels by controlling the local composition may prove to be particularly useful in the production of memristor circuits. That technology depends on the ability to have controlled resistance changes. Understanding the fundamental mechanisms governing ion migration in HPs and the development of methods that can synthesize and modify the materials and structures are critical areas of research that may enable the realization of practical perovskite based synaptic devices.

### 3.5. *Photoinduced halide-ion segregation in mixed-halide perovskites*

With their soft lattice and high ionic diffusivity, light illumination on mixed-halide perovskites can induce halide-ion segregation. This can result in domain formation, along with corresponding changes to the material's optical and electrical response. Furthermore, this phenomenon, depending on various condition on HPs such as grain size and halide composition, can be controlled by annealing process [117]. Studies by the X-ray diffraction (Fig. 7(c)) [115], as well photoluminescence, cathodoluminescence, transient differential absorption, and elemental analysis have reported analogous results. Due to the small activation energies for migration in these halide ion materials, such light-induced segregation occurs quickly, typically within seconds. Fig. 7(d) shows the schematic Helmholtz free-energy curves of $MAPb(Br_xI_{1-x})_3$ mixed-halide in the light and in the dark predicting phase segregation and energy diagram sketches of the relative band gaps of each phase [116]. The red dashed lines show that the lowest attainable free energy in the light occurs when the material segregates into I-rich and Br-rich phases, while the blue dashed line shows that the lowest energy is attained when the material remains in a single phase in the dark.

The salient features of phase segregation in $MAPb(Br_xI_{1-x})_3$ mixed-halide include: 1) the rate of phase segregation increases with increasing excitation light intensity and saturates at a critical light intensity, and 2) there exists an excitation intensity threshold below which no phase separation occurs [118]. The authors proposed a model suggesting that the driving force behind phase separation is the bandgap reduction of iodide-rich phases. The model also explains observed nonlinear intensity dependencies of phase segregation, as well as self-limited growth of iodide-rich domains. Engineering carrier diffusion lengths and injected carrier densities are suggested to stabilize against phase separation.

Because bandgaps and conductivities vary with HP compositions, this photoinduced phase segregation might be used to change synaptic weight. Another more interesting aspect is that the halide-ion segregation is reversible, and the original state can be slowly restored after removing the stimulation. Hence, combining the photoinduced halide-ion segregation of mixed-halide perovskites with light-stimulated synapses may open opportunities for the implementation of bionic sensory adaptation, useful in machine-human interface and robotics applications.

## 4. HP-based synaptic devices

### 4.1. *Memristors*

Memristors [119,120], or resistive memory, with their simple two-terminal structure, highly dense integrability, and fast switching speed, have attracted much attention as artificial synaptic devices. This is particularly true for RRAM devices.

Depending on the choice of the perovskite material and the electrode, the resistive switching (RS) characteristics in HP memristors can be classified as filamentary and interface types, as in other memristors. Filament-type resistive switching is caused by formation of conductive filaments through redox reaction or ionic migration. The filament is formed in the electroforming SET process that changes the medium from a high resistance state (HRS) to a low resistance state (LRS). It is dissolved when the medium goes back from LRS to HRS in the RESET process. Two mechanisms govern the filament formation: electrochemical metallization

(ECM) [121,122] and valence state change mechanism (VCM) [123,124]. ECM based memristors, so called conductive bridging RAM (CBRAM), rely on electrochemically active metal (Ag, Cu, Ti, Ni) as one electrode and an inert counter electrode. The migration of these active metal ions results in formation or rupture of the conductive filaments. In contrast, VCM is generally an area-dependent phenomenon and the valence state of the active material close to the electrode can be changed by anion migration and redistribution, and the resulted Schottky barrier change leads to current flow on or off.

HP-based filament-type memristor devices have been widely investigated for artificial synapse applications [43,44,125–127]. Zeng et al. reported the filament-type resistive switching in an all-inorganic $Cs_3Cu_2I_5$ perovskite thin film fabricated by a solution-based method [125]. The memristor has a structure of Ag/$Cs_3Cu_2I_5$/ITO in which PMMA act as an isolating layer to separate the Ag electrode from the $Cs_3Cu_2I_5$ thin film (Fig. 8(a)). The device exhibits a bipolar resistive switching behavior with low SET/RESET voltages (Fig. 8(b)). An electroforming step is needed to activate the device. The conduction mechanism is revealed in Fig. 8(c) and (d). The LRS state follows the Ohmic law as a result of the formation of Ag conductive filament whereas the HRS state follows the Child law and trap-free space charge limited conduction, depending on the voltage. Fig. 8(e) illustrates the resistive switching mechanism. With a positive bias, Ag atoms are oxidized ($Ag \rightarrow Ag^+ + e^-$) and these $Ag^+$ cations move toward the ITO electrode. Simultaneously electrons from the Ag electrode move toward the ITO electrode in the external circuit to reduce $Ag^+$ and form the Ag filament between the two electrodes. The filament is dissolved in a reverse process under negative bias during the RESET process. Synaptic behaviors, including LTP/LTD, have been investigated and surprisingly, these filament-type memristor devices show reasonable linearity when driven in the pulse mode. However, their endurance is quite low.

Ku et al. demonstrated multi-level analog resistive switching with a hybrid perovskite $MAPbX_3$ memristor [44]. A multi-level analog SET/RESET process and a digital SET/analog RESET process from this work are depicted in Fig. 9(a) and (b). In that study, the Ag cations naturally form the $\beta$-AgI phase and act as an Ag cation reservoir at the interface between the Ag electrode and $MAPbI_3$ [44,125]. The Ag atoms can easily move into $MAPbI_3$ via the $\beta$-AgI interlayer under the positive bias voltage, causing the formation of Ag conducting filaments (CFs). When an appropriate voltage is applied, the migration of Ag atoms toward the opposite electrode is favorable for the multilevel analog switching states. A gradual increase and decrease in the conductance states under consecutive positive and negative pulses are observed, corresponding to the potentiation/depression synaptic behaviors, which result from the formation of multiple Ag CFs during the electroforming step. Their devices also successfully emulate the fundamental synaptic characteristics of biological systems, such as spike-rate-dependent plasticity, paired-pulse facilitation, post-tetanic potentiation, transition from short-term memory to long-term memory, and spike-timing dependent plasticity.

In addition to cation-based filamentary switching, the filaments in HPs can be formed by anion species or point defects migration [43,128–130], similar to oxygen ions in metal oxides [131,132]. The formation of vacancy-based CF is dependent on its migration energy. $I^-$ ions migrate with a small activation energy. This results in the generation of a large concentration of $V_I$ in $MAPbI_3$, as mentioned earlier, which can form vacancy-based CF. If an electrochemically active electrode is used, such as Ag or Cu, the corresponding cations $Ag^+$ and $Cu^{2+}$ would be possible to migrate through the medium layer to form metallic CFs. However, this may depend on the thickness of the HP layer. For the same Ag/$MAPbI_3$/FTO structure [44], the memristor devices are found to exhibit different type of CFs, depending on the $MAPbI_3$ thickness [128]. Fig. 9(c) shows typical *I–V* characteristics of this structure with $MAPbI_3$ thicknesses in a range from 90 to 300 nm. The SET voltage is reduced with decreasing $MAPbI_3$ thickness. For the 90 nm-thick device, its LRS resistance is an order of magnitude lower than that of 150, 240, and 300 nm-thick device. When the $MAPbI_3$ layer thickness is hundreds of nanometers, the diffusion and formation processes of $V_I$ CFs dominates the resistive switching behaviors.

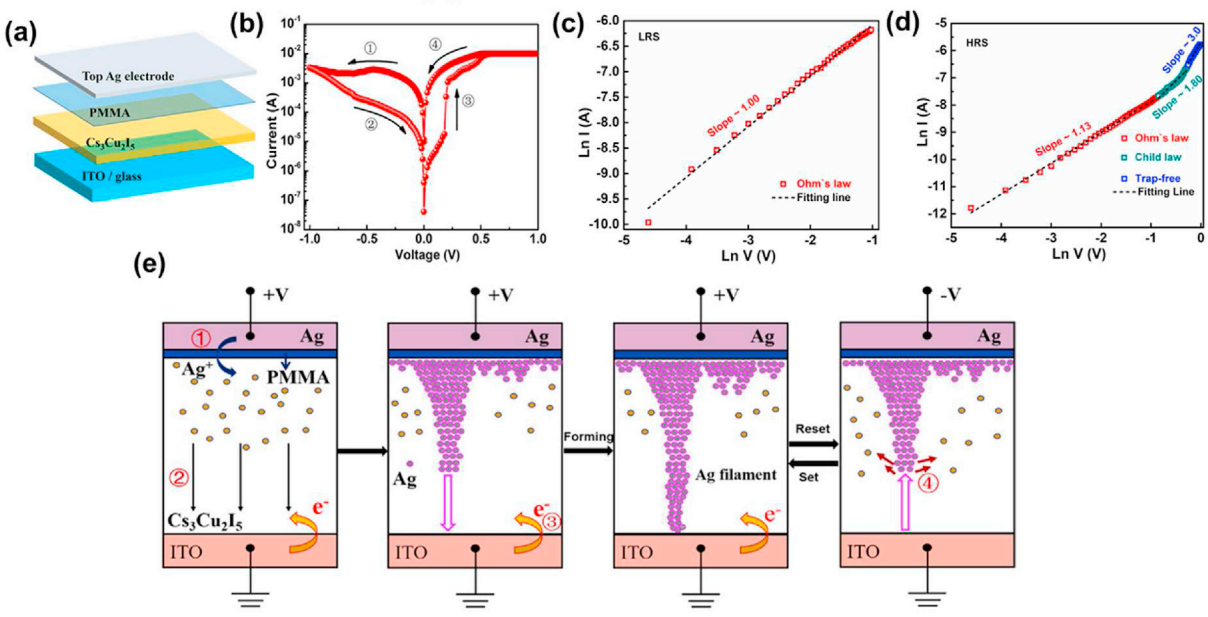


**Fig. 8.** (a) Schematic of the Ag/PMMA/$C_3Cu_2I_5$/ITO memristor vertical stack structure. (b) Bipolar-RS *I–V* characteristic. Conduction mechanism of the $C_3Cu_2I_5$ based memristor: (c) LRS, (d) HRS. (e) Schematic illustration of the formation/rupture of the Ag filament under the electrical field. Reproduced with Permission [125]. Copyright 2020, American Chemical Society.

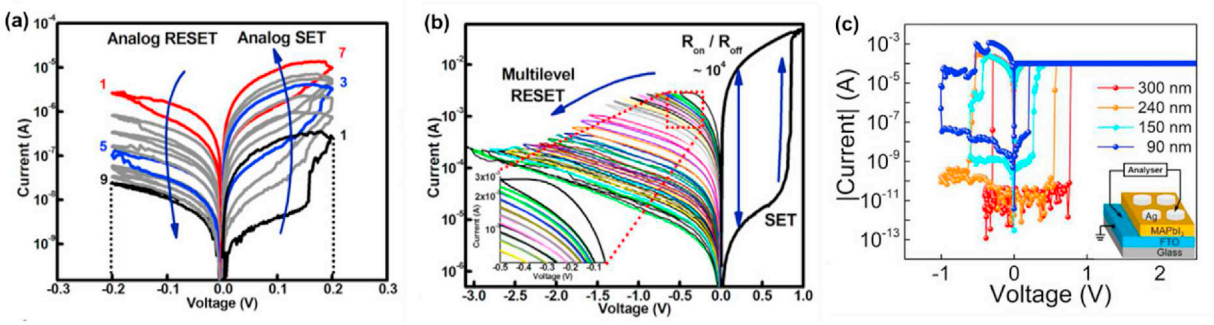


**Fig. 9.** RS *I*–*V* characteristics of Ag/$MAPbI_3$/FTO memristor: (a) analog SET/RESET process under low voltage sweeps, (b) digital SET and multilevel RESET process under high voltage sweeps. Reproduced with Permission [44]. Copyright 2020, Elsevier. (c) Typical *I*–*V* characteristics of the Ag/$MAPbI_3$/FTO memristors of different thicknesses (90, 150, 240, and 300 nm). Reproduced with Permission [128]. Copyright 2018, American Chemical Society.

The Ag CFs emerge and coexist with $V_I$ ones as the HP layer thickness is reduced to ~90 nm. The resistance-temperature characteristic of the 90 nm-thick device reveals its metallic conductivity [133,134], in contrast to 300 nm-thick cells that are dominated by vacancy conductivity [135,136]. Auger electron spectroscopy (AES) depth profiles of Ag and I atomic concentrations also confirm this conclusion.

Another mechanism for the RS in HP memristor is interface-type RS. This mechanism is based on the homogenous modulation of the Schottky barrier at the electrode/HP interface through formation and subsequent accumulation of ions [137–139]. In their work using the Au/$MAPbBr_3$/ITO structure [137], Guan. et al. reported that MA vacancy ions ($V_{\bar{MA}}$) are the most likely cause of the modulated Schottky barrier under an electric field. When there is no external bias, more vacancies in the as-prepared HP layer are located near the perovskite/ITO interface, as revealed by EELS measurements, and the Schottky barrier height (SBH) limits the junction current (Fig. 10(a)). With increasing negative bias on the Au electrode, the junction current initially increases quickly because the junction is in the forward bias condition (Fig. 10(b)). However, under the forward bias, the diffusible negative ions ($V_{\bar{MA}}$) drift towards the ITO electrode and accumulate near the perovskite/ITO interface. This enhances the SBH and then reduces the current. On the other hand, with a positive bias on the Au electrode, the junction is in the reverse biased condition and the current decreases (Fig. 10 (d) and (e)).

The Schottky barrier can also be modulated by charge trapping and de-trapping into interface trap centers [139–141]. Zhou et al. investigated a trap-mediated switching behavior in an Au/$MAPbI_{3-x}Cl_x$/FTO memristor. For this device, the Schottky contact at the HP/Au interface is formed due to their work function differences and surface states [139]. When a positive bias is applied to the Au electrode, the Schottky barrier is lowered as a result of the injected holes from the Au electrode being captured by trapping centers. This caused a quasi-ohmic state and changes the resistance to an LRS. With a negative bias, holes are ejected from the trap states to the Au electrode, and the resistance is switched back to the HRS.

The representative HP-based memristors for artificial synapses and their basic performance are summarized in Table 1.

### 4.2. Memcapacitors

Memcapacitors exhibit switchable capacitance [142]. They are emerging as an attractive candidate for high-density information storage due to their multilevel, changeable capacitances and long-term retention. Similarly, they are also an attractive candidate for artificial synapses. Studies have reported that the memcapacitive behavior in a material system is concurrent with their memristive

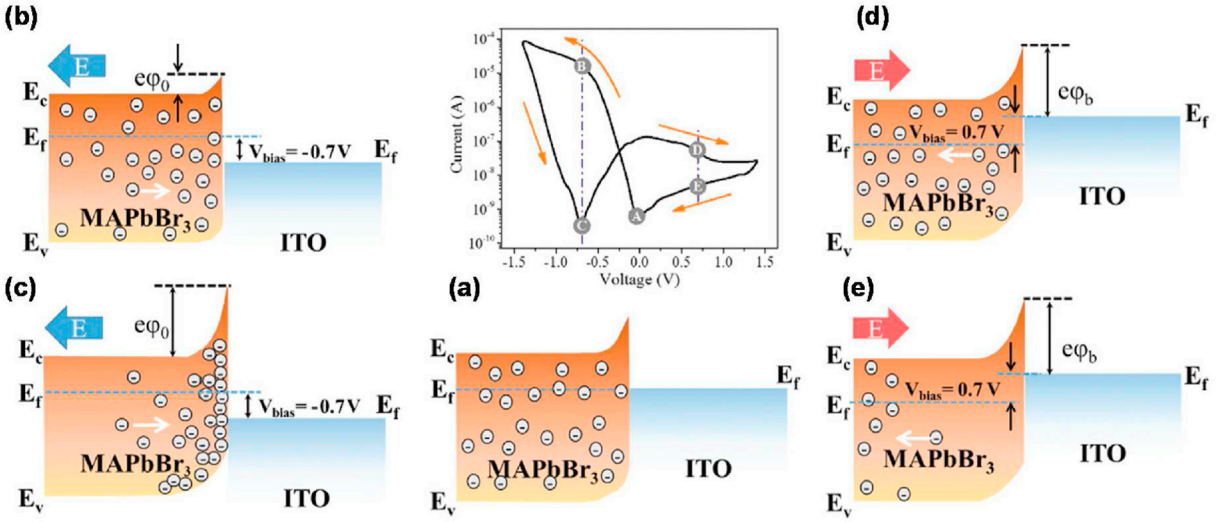


**Fig. 10.** Interface-type RS mechanism in HPs. Schematic illustrations of ion migration at the $MAPbBr_3$/ITO interface during RS switching process. (a)–(e) are the conditions at specific points in the *I*–*V* characteristics, which is related to ion redistribution and the modified Schottky junction. Reproduced with Permission [137]. Copyright 2017, Wiley-VCH.

**Table 1**
Memoristive perfermances and switching mechanisms of various HP-based memristors.

| Device Structure | Switching mechanism | $V_{SET}/V_{RESET}$ (V) | On/Off ratio | Endurance (cycles) | Memory retention(s) | Ref. |
|---|---|---|---|---|---|---|
| Ag/$CsSnI_3$/Pt | Ag filamentary | 0.13/−0.08 | $7 \times 10^3$ | 600 | $7 \times 10^3$ | [138] |
| Ag/PMMA/$Cs_3CuI_5$/ITO | Ag filamentary | 0.6/−0.44 | $10^2$ | 100 | $>10^4$ | [125] |
| Ag/$MAPbI_3$/FTO | Ag filamentary | 0.9/- | $10^4$ | $>10^3$ | $4 \times 10^4$ | [44] |
| Ag/$MAPbI_3$/FTO | Ag/$V_I$ filamentary | 0.8/−0.3 | $10^6$ | $10^3$ | $10^5$ | [128] |
| Au/$MAPbI_3$/ITO | $V_I$ filamentary | 0.7/−0.7 | ~10 | 400 | $10^4$ | [130] |
| Ag/$MAPbI_3$/Pt | $V_I$ filamentary | 0.13/−0.13 | $>10^6$ | 360 | $10^4$ | [127] |
| Ag/$MAPbI_{3-x}Cl_x$/FTO | Ag filamentary | 2/−2 | 30 | $3 \times 10^4$ | $>4 \times 10^4$ | [126] |
| Ag/PMMA/$MA_3Sb_2Br_9$/ITO | Sn/$V_{Br}$ filamentary | −0.5/1.2 | $10^2$ | 300 | $>10^4$ | [43] |
| Au/PMMA/$CsSnI_3$/Pt | $V_{Sn}$ Interface-type | 0.45/−0.6 | $5 \times 10^2$ | <120 | – | [138] |
| Au/$MAPbI_{3-x}Cl_x$/ITO | Interface-type | 1.47/-1.41 | $10^4$ | 50 | $4.32 \times 10^4$ | [139] |
| Au/$MAPbBr_3$/ITO | Interface-type | –/– | $10^3$ | $10^3$ | $10^4$ | [137] |

switching [143,144]. Thus HPs, with their obvious memristive behaviors, might also be candidates for memcapacitors.

One unique feature of HPs for capacitive devices is their giant dielectric constant [90,145–149]. In a study of the dielectric constant in $MAPbI_{3-x}Cl_x$ under various operating conditions including bias voltage, illumination, and temperature, an extremely large static dielectric constant ($\varepsilon_0 > 1000$) was measured, even in the dark [90]. Under light illumination, the dielectric constant can increase to $10^6$ as a result of a material structural fluctuation caused by rotation of the polar MA cation or ionic off-centering. By evaluating the capacitance response of $MAPbI_3$ as a function of frequency and temperature [146], two main polarization processes are identified: (1) dielectric changes in the microscopic dipolar units in the measured intermediate frequency range from the orthorhombic-to-tetragonal phase transition (this accounts for capacitance) and (2) electrode polarization at small frequencies from interfacial effects, presumably related to kinetically slow ions piled up in the vicinity of the outer interfaces.

Qian et al. demonstrated the memcapactive characteristic in Au/$MASnBr_3$/ITO structure that resulted from Br ion migration [150]. As shown in Fig. 11(a), their memcapacitors can be modulated between four stable capacitive states, ON1 (60 pF), ON2 (95 pF), ON3 (140 pF) and OFF, by increasing sweep voltages from up to 5 V. These states can be retained well above the $10^4$ s range at a bias of 0 V and 1 MHz frequency (Fig. 11(b)). Fig. 11(c) shows a step-like capacitance change with frequency and temperature caused by different dielectric relaxation processes [145–148,151,152]. The memcapacitive switching stems from the modulated p–i–n junction capacitance triggered by $Br^-$ migration, as demonstrated by *in-situ* element mapping, X-ray photoelectron spectra, and frequency-dependent capacitance measurements.

Studies on HP-based memcapacitors are still considerably rare [153,154]. However, the unique combination of both a large dielectric constant and its tunability by external stimuli in HPs could render this material system an excellent candidate for memcapacitors, suitable for synaptic applications.

### 4.3. Synaptic phototransistors

In addition to two-terminal memristor and memcapacitor based synaptic devices, three-terminal synaptic transistors [18,155–157] have been actively investigated, largely because of their very small power consumption [158,159] and simultaneous information processing and learning capability. Such devices have advantages over two-terminal devices in which the same terminal is used for reading and writing and thus cannot simultaneously carry out processing and learning steps together.

Synaptic phototransistors, by introducing photo control, further expand the functions of synaptic transistors. In such optoelectronic synapses, the ability to modulate synaptic plasticity is more significant for the "optical" programming scheme when compared to its "electrical" counterpart. More interestingly, they offer the possibility for mimicking human visual memory. Most implements adopt a photogate configuration, in which the photosensitive gate is coupled to the channel through an insulator or a type-II heterojunction. Photogenerated electrons or holes are injected into the channel to program its conductivity, which acts as the synaptic weight, while the opposite carriers are accumulated in the floating gate to change the transistor threshold voltage (photogating effect). HPs have superior optoelectronic properties, including a small exciton binding energy, strong absorption coefficient, high charge carrier mobility, and long charge carrier lifetime, and therefore, are particularly suitable as the photosensitive gate [36,160–165]. In addition, synapses with a photosensitive HP channel configuration are also reported.

Wang et al. demonstrated various synaptic behaviors with a Si/

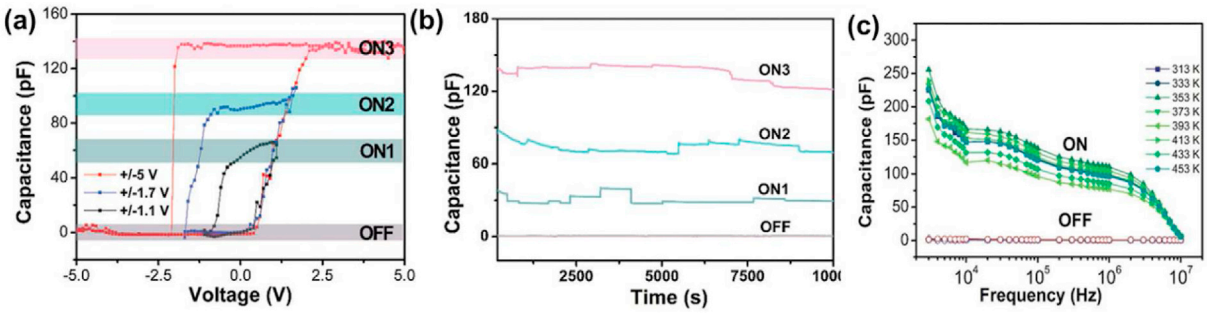


**Fig. 11.** (a) Quaternary *C–V* characteristics of a memcapacitor with ITO/$MASnBr_3$/Au structure under the voltage sweeps $-V_{max} \rightarrow 0 \rightarrow V_{max} \rightarrow 0 \rightarrow -V_{max}$, where $V_{max}$ increases from 1.1, 1.7–5 V. (b) Retention characteristics of four capacitive states read at 0 V and 1 MHz. (c) Frequency- and temperature-dependency of the capacitance. Reproduced with Permission [150]. Copyright 2019, Wiley-VCH.

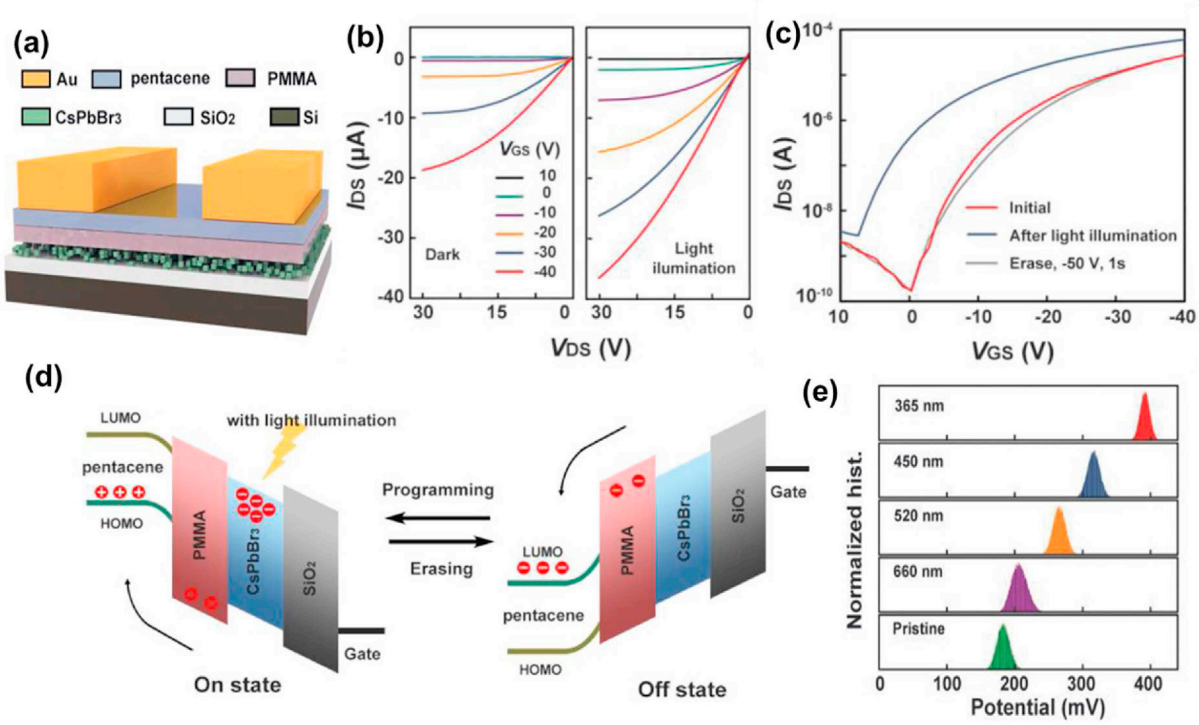


**Fig. 12.** (a) Schematic illustration of the $CsPbBr_3$ QDs-based photonic transistor. (b) Output characteristics of the transistor in the dark and under light illumination condition (light wavelength: 365 nm, light intensity: 0.153 $mWcm^{-2}$). (c) Transfer characteristic ($V_{DS} = -30$ V) of the $CsPbBr_3$ QDs-based photonic transistors. (d) Schematic energy diagram of the device during light programming operation and during electrical erasing operation under dark condition. (e) Surface potential of the $CsPbBr_3$/PMMA/pentacene film before and after different light illumination treatments (fixed light intensity: 0.153 $mWcm^{-2}$) recorded by in situ KPFM. Reproduced with Permission [36]. Copyright 2018, Wiley-VCH.

$SiO_2$/$CsPbBr_3$ quantum dots/PMMA/pentacene/Au structure using photonic programming and electrical erasing process (Fig. 12(a)) [36]. The device in the dark has an on/off ratio of ~$10^5$. The enhancement of drain current was observed under illumination and the threshold voltage shifts in the negative direction (Fig. 12(b) and (c)). Under illumination, photogenerated electrons are accumulated in $CsPbBr_3$ QDs, which serve as a floating gate, and photogenerated holes are injected into the *p*-type pentacene channel layer, causing the increasing channel conductance (Fig. 12(d)). The authors verified the charge trapping/releasing mechanism through in situ KPFM by varying the light wavelength (Fig. 12(e)) and confirmed that the increase in surface potential is caused by aggregation of holes.

Periyal et al. reported a thin-film transistor-like synaptic device comprised of all-inorganic cesium lead bromide ($CsPbBr_3$) perovskite quantum dots (QDs) and amorphous indium gallium zinc oxide (IGZO) semiconductor active material (Fig. 13(a)) [160]. $CsPbBr_3$ QDs are used to make a photosensitizer. The photoelectron injection into IGZO is performed using the type II heterostructure between QDs, and the IGZO serves as a basis for electro-optical programming. Injection of photoelectrons into IGZO increases the channel conductance and shifts the threshold voltage ($V_{th}$) of channel formation, while photo-holes trapped in $CsPbBr_3$ act as a positively biased gate. After light illumination is removed, the channel conductivity exhibits persistent photoconductivity with a very slow decay rate. With light-induced charge trapping (optical mode) and electric-induced charge releasing (electrical mode) properties, the device can be optically programmed and electrically erased. In the electrical mode, the drain current can be altered temporarily by charging carriers at the interface, wherein holes

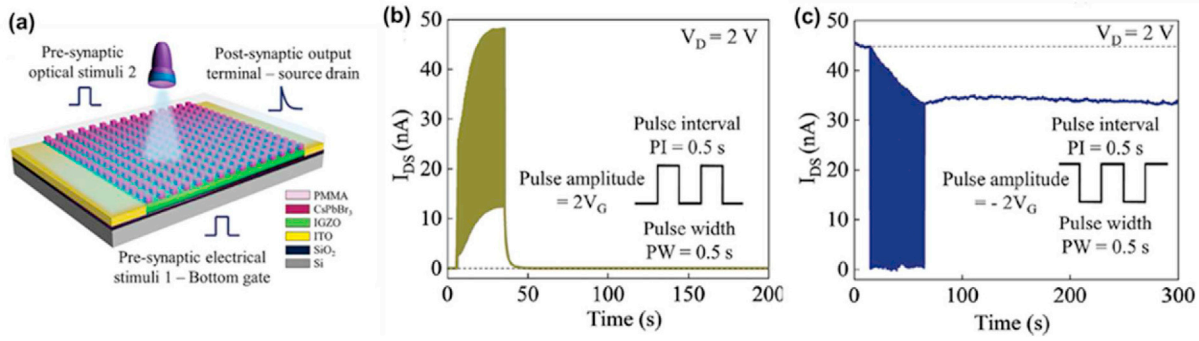


**Fig. 13.** (a) Schematic of $CsPbBr_3$ QDs-IGZO based photonic transistor as an artificial synapse. Drain current modulation under the electrical mode, mimicking (b) short-term potentiation and (c) long-term depression. Reproduced with Permission [160]. Copyright 2020, Wiley-VCH.

occupy shallow, and electrons occupy deeper traps. The device thus has a short-term increase and a long-term decrease in drain current (Fig. 13(b) and (c)). In contrast, illumination exhibits a long-term increase. These changes in drain current rely on electrical and optical pulse parameters including pulse width, amplitude, interval, and number of repetitions. The device shows a wide dynamic range of synaptic weight modulation. Learning rules such as STDP, associative learning, and linear nonvolatile blind updates have also been demonstrated, suggesting their compatibility with both SNN and DNN computing architectures.

In addition to their sensitivity to light illumination, another desirable property of HP-based transistors, ambipolar switching, can be utilized to attain a wide range of synaptic weight [166–168]. Here HPs are used as the photosensitive channel of phototransistors. Fig. 14(a) and (b) show the $MAPbI_3$-based phototransistor structure which exhibits ambipolar carrier transport characteristics, *i.e.*, they work in both accumulation (*p*-type) and depletion (*n*-type) modes [166]. In the dark condition, the drain current remains below 0.5 nA while it abruptly increases by 0.1 mA under illumination, giving $I_{D,light}/I_{D,dark} = \sim 10^6$. With illumination, $I_{on}/I_{off}$ is $\sim 10^4$. The device exhibits fast optical response (<10 μs). Furthermore, the gate voltage can be used to control the drain current. Although such a phototransistors should be combined with additional materials [161] to separate excitons for LTP implementation, the device shows stable and fast short-term memory characteristics. Fig. 14 (c) and (d) displays output characteristics in light, operated in hole-enhancement and electron-enhancement modes, respectively.

In addition to the conventional phototransistor structure, other structures have also been investigated to achieve photonic resistive switching memory functions. For instance, Guan et al. [169] reported a multilayer architecture of ITO/$MAPbBr_3$/Au/$MAPbBr_3$/Ag, in which, the bottom ITO/$MAPbBr_3$/Au sandwich serves as a photodetector, and light illumination modulates the voltage distribution, which controls the resistive states of the top Au/$MAPbBr_3$/Ag resistive switching device. Another photonic RS memory is reported in Ref. [170] with a bilayer structure of strontium titanate (STO) QDs and halide perovskite CsPbBr3 (CPB). This bilayer device shows improved RS performance with a high switching ratio and long retention time. The formation of heterojunction between STO and CPB significantly enhances the high resistance state, and the separation of the active silver electrode and the CPB layer contributes to the long-term stability.

## 5. Performance of HP-Based artificial synapses

### 5.1. For DNN applications

The most important device parameters for artificial synapse used in DNNs are multilevel states, dynamic range, symmetry/linearity of weight update, retention/endurance, program energy consumption, and device size [34]. Generally, more states (e.g. > 100) could be translated into a better learning capability and an improved network robustness. If the number of states is insufficient, multiple devices can be grouped as one device to meet the precision requirement. Dynamic range is the ratio of the maximum and minimum conductance of artificial synapses, which is closely related to the number of states. The larger the dynamic range is, the better mapping capability of the weights in the algorithm to the conductance in the device. Most synaptic devices have a range of 2–100. The weight update characteristics should be linear and symmetric, especially for online training. However, most devices have a tendency to change conductance rapidly at the beginning and then saturate at the end of the process, resulting in a nonlinear and asymmetric response while the weight increases or decreases. They also should have high cycle endurance and long data retention. After training is completed, the synaptic devices should behave as a static memory with a data retention on the order of ten years at ~85 °C. Biological synapses consume an estimated energy of 1–10 fJ per event, a value that artificial synaptic devices should strive to achieve. The device size determines the ultimate integration density, and a sub-10-nm regime is another target worth pursuing.

Ham et al. [171]. fabricated Ag/$CH_3NH_3PbI_3$/ITO photonic synapses capable of accelerated learning at low power. Thanks to photon-accelerated iodine vacancy migration, the HP synaptic device exhibits light-tunable synaptic functionalities with a programming voltage of only 0.1 V. Interestingly, with photon excitation, the LTP threshold in those devices decreased. 3-layer DNN with backpropagation training was simulated using the measured device parameters to verify if this HP-based synaptic device could be useful for DNN applications. Fig. 15(a) shows the 3-layer DNN configuration designed to recognize "3", a large MINST handwritten digit with 28 × 28 pixel form. The DNN architecture consists of 784 input neurons (28 × 28 pixels), one hidden layer, and 10 output neurons to recognize 0–9 ten digits. Fig. 15(b) shows the dependence of recognition accuracy on the training phase. With only potentiating and depressing pulses at 0.15 V and −0.28 V respectively, ~10% of the accuracy is achieved after 4500 learning

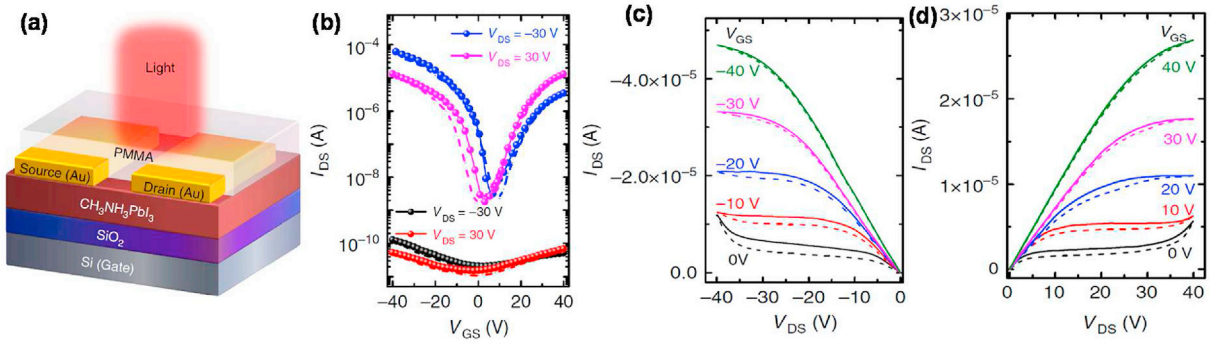


**Fig. 14.** Ambipolar characteristics of the hybrid perovskite phototransistors as artificial synapses. (a) Schematic of the phototransistor with a channel of hybrid perovskite $CH_3NH_3PbI_3$. (b) Its transfer characteristics in the dark (black and red symbols) and under light illumination (blue and magenta symbols). (c, d) Respective output properties of the device under light condition. Reproduced with Permission [166]. Copyright 2015, Nature Publishing Group. (For interpretation of the references to colour in this figure legend, the reader is referred to the Web version of this article.)

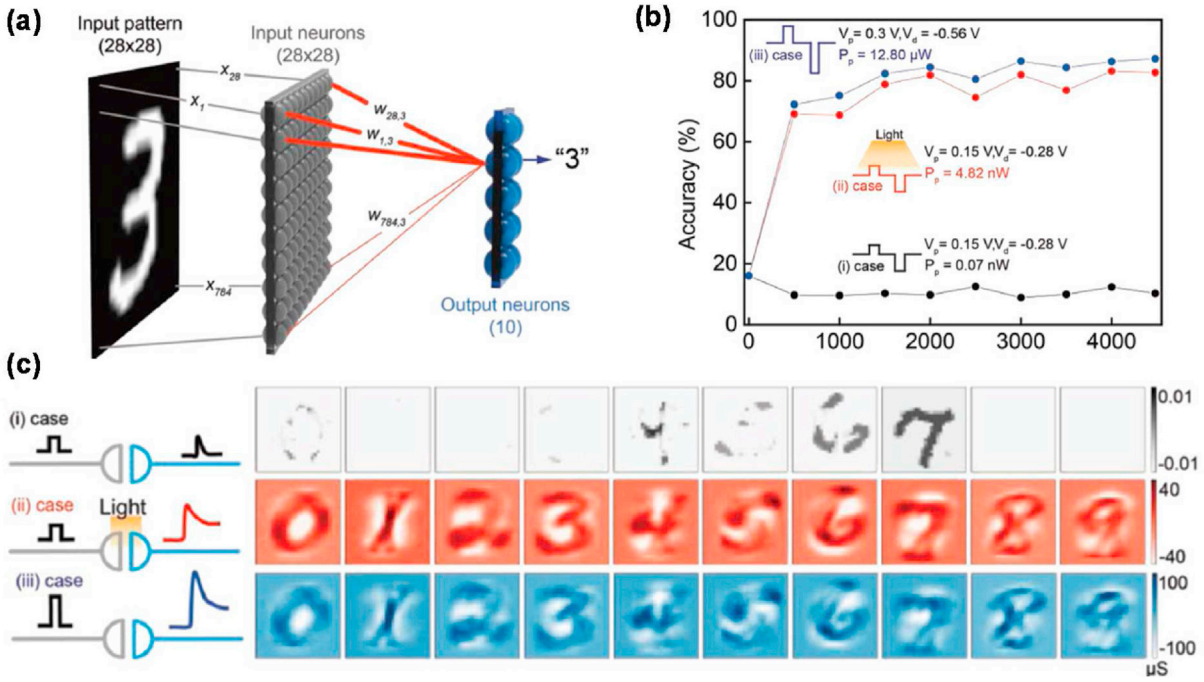


**Fig. 15.** (a) Schematic of a 3-layer DNN to recognize the handwritten "3". (b) Recognition accuracy for the MNIST patterns as a function of the number of learning phases according to three cases. (c) Reshaped 28 × 28 contour images of the final synaptic weights corresponding to the MNIST patterns after 4500 learning phases for the three cases. Reproduced with Permission of [171]. Copyright 2018, Wiley-VCH.

cycles ((i) case: black points), suggesting that LTP/LTD cannot be implemented. In contrast, by adding light pulses ((ii) case) or applying higher amplitude electrical pulses ((iii) case), a much higher pattern recognition accuracy of 83% can be achieved. Fig. 15(c) shows the reshaped 28 × 28 contour images of the final synaptic weights corresponding to the MNIST patterns after 4500 learning phases for the three cases. The results indicate that the pulse variables, in addition to the linearity on potentiation/depression behaviors as a function of number of pulses, are crucial factors to achieve higher recognition accuracy. The study also shows the energy consumption can be lowered using a combination of electrical and optical pulsing.

Many other phototransistor structures have been reported for similar applications. For instance, 2D layered HP/oxide semiconductor-based broadband optoelectronic synaptic transistors with long-term visual memory was reported by combining 2D-$(C_4H_9NH_3)_2PbBr_4$ with indium zinc oxide (IZTO) [172]. Such an optical synapse can perceive and memorize optical information with long-term retention for using in neuromorphic visual systems.

In Ref. [173], Kim et al. reported that vertically aligned 2D halide perovskites (V-HP) synapses show positive and negative analog conductance changes that are modulated by driving pulses, emulating synaptic potentiation and depression. A 3-layer DNN with backpropagation training with the measured device parameters was simulated to verify if this HP-based synaptic device could be useful in DNN applications, as shown in Fig. 16. In addition to the common small and large MINST handwritten digits, 28 × 28 pixels of ten clothing images (T-shirts, trousers, pullover, dress, coat, sandal, shirt, sneaker, bag, and ankle boot), known as Fashion MNIST (Fig. 16(a)) was also used for testing. The network optimizes the best-deduced model by updating synaptic weights extracted from the measured conductance state properties (Fig. 16(b–d)). The nonlinearity of potentiation and depression is extremely small, and the 50 times cycle-to-cycle potentiation and depression result confirms that the V-HP synapses is reliable and exhibits low noises. Astonishingly, with 60,000 training sets and 10,000 testing sets, this V-HP-based DNN can achieve an 86% accuracy for Fashion MNIST recognition (Fig. 16(e)), within 3% of the theoretical limit for floating-number-based neural network performance. Remarkably high accuracies of up to 95.2% in small MNIST and 96.5% in large MNIST recognition is also achieved with this DNN after 60,000 training sets, within <1% of the theoretical limits. These impressive numbers are attributed to the V-HP synapses' highly linearity and low noise. This results in extremely efficient and accurate analog tuning of the synaptic weights.

### 5.2. For SNN applications

The characteristics of a synaptic device for SNNs can be identified from its STP/STD and LTP/LTD behaviors. Synaptic STP enhancement is mainly time-dependent, divided into (1) facilitation (milliseconds to second), (2) augmentation (a few seconds), and (3) potentiation (10 s to minutes) phases [174–176]. Fig. 17(a) shows enhancement and drops in $CsPbBr_3$-based artificial synaptic device current that result from exposure to a series of pulses that modify the synaptic weight (conductivity) [177]. Application of a series of positive voltage pulses as excitatory stimuli causes the current to gradually increase in the potentiation process, while a series of negative voltage pulses causes it to recede back to its initial value during the depression process. One feature of STP is paired pulse facilitation (PPF), which indicates that the postsynaptic current further increases when the interval between two consecutive spikes ($\Delta t$) decreases [36,37,178]. As shown in Fig. 17(b), when the interval is much longer, the altered synaptic weight diminishes back to its initial state. Thus, the PPF index (A2/A1) reaches 100%. However, the current (A2) further increases as the interval is shorter and the modulated synaptic weight remains unchanged within several hundred milliseconds as a short-term memory (STM). In general, the PPF effect relies on spike parameters that include amplitude, duration time, and number of repetitions

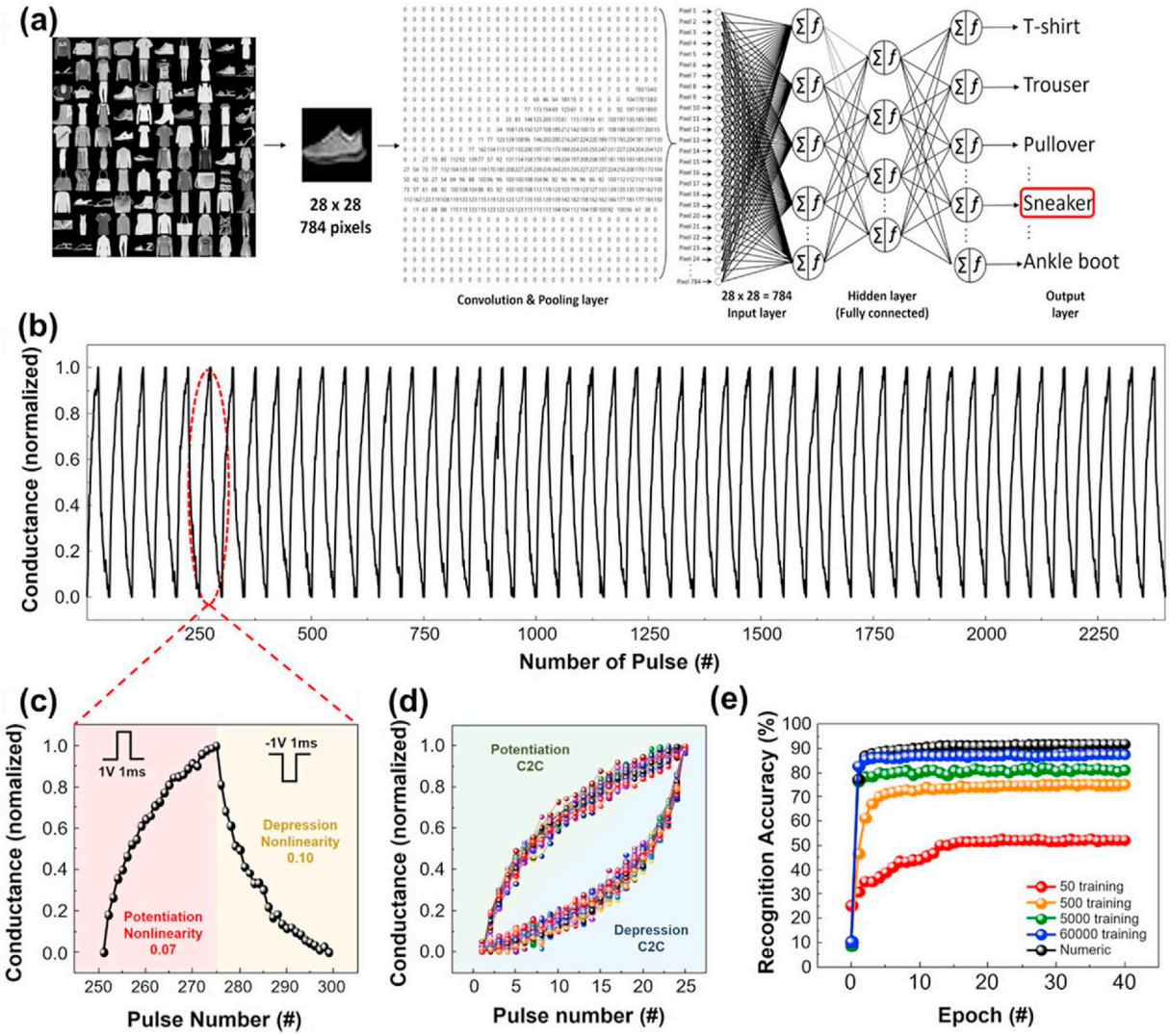


**Fig. 16.** (a) Data processing flow chart of an DNN for learning Fashion MNIST image data. (b) Synaptic conductance potentiation and depression with symmetry. (Potentiation: 25 pulses with +1 V amplitude and 1 m s duration, depression: 25 pulses with −1 V amplitude and 1 m s duration, repeated 50 cycles) (c) Potentiation and depression synaptic characteristics showing high linearity. (e) 50 times cycle-to-cycle programmable synaptic conductance with extremely low noise. (f) Recognition accuracy in Fashion MNIST of V-HP based network and floating-number-based network (numeric) depending on the training sets. An epoch indicates the number of passes of the entire training dataset completed by the deep learning algorithm. Reproduced with Permission [173], Copyright 2021, Elsevier.

[36,163,179]. The PPF effects have also been reported for $APbBr_3$ with different A-site cations. Variation of A-site cation can tune the activation energy and hence control vacancy-mediated ion migration [37]. The biological synapses-like PPF characteristic of artificial synapses has been applied for simple learning and information processing [174], and for determining the direction of a sound source [175].

LTP in biological neuron-synapse networks can be generated through a strong depolarization from more intensive spikes. Especially, STDP based on Hebbian learning rule [41] have been widely studied for implementing pattern recognition in SNN as well as in DNN. Synaptic weight can be altered using the relative timing of action potentials applied to pre-/post-synapse, which is based on associative learning and information storage. In other words, the synaptic weight changes $\Delta w$ are a function of $\Delta t$. STDP exhibits different types, varying with frequency or number of repetition of spikes, or the type of synaptic spikes: excitatory or inhibitory [37,39,180,181]. By modifying the shape of the pre-synaptic and post-synaptic spikes, Xiao et al. demonstrated four different forms of STDP in their measurements of the Au/$MAPbI_3$/PEDOT:PSS/ITO structure [180]. For instance, in the case of the most common asymmetric Hebbian STDP rule, LTP can be realized when a pre-synaptic spike fires before a post-synaptic spike ($\Delta t > 0$), while LTD can be formed when a post-synaptic spike precedes a pre-synaptic spike ($\Delta t < 0$), as shown in Fig. 17(c). However, in an asymmetric *anti*-Hebbian rule, both LTP and LTD occur but with a reverse relationship to spiking timing when compared to asymmetric Hebbian rules (Fig. 17(d)). The synaptic weight change can be further tuned as the spike timing difference is shortened. The symmetric Hebbian and *anti*-Hebbian learning rules are also demonstrated in this HP-device (Fig. 17(e) and (f)).

Memory retention, the period in which the changed synaptic weights are maintained, is an essential feature for implementation of artificial synapses. According to the multi-store model suggested by Atkinson and Shiffrin [182], the input information registered as sensory memory is transferred to STM temporarily by storing the information through attention, and then finally transited to long-term memory (LTM) through repeated rehearsal. The memory

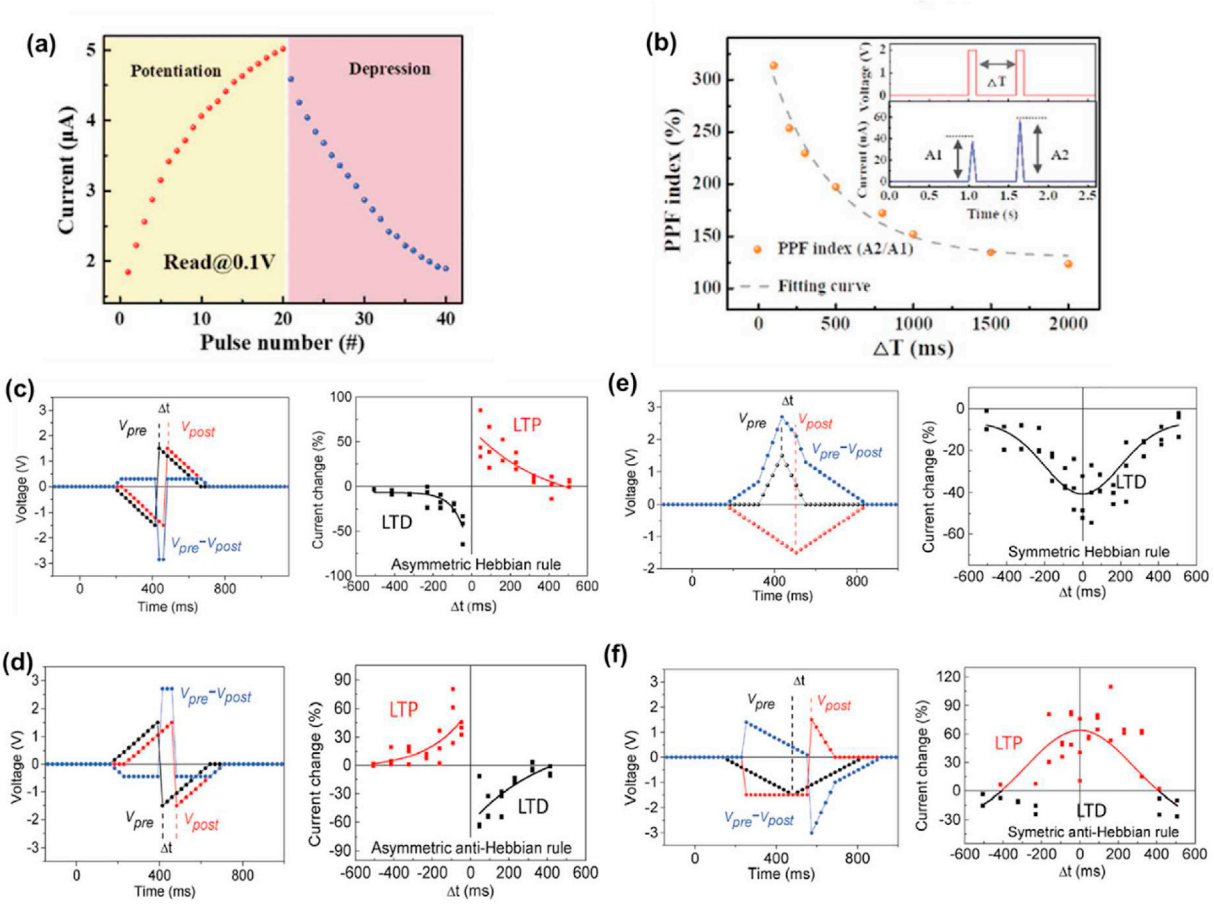


**Fig. 17.** (a) Synaptic potentiation and synaptic depression triggered by electric stimuli. (b) Electrical PPF index versus time interval between successive pulses. The inset shows the paired-pulse facilitation phenomenon, emulating a biological process of PPF. Reproduced with Permission [177]. Copyright 2020, Wiley-VCH. Different STDP characteristics of $MAPbI_3$ based memristor: (c) Asymmetric Hebbian rule, (d) asymmetric *anti*-Hebbian rule, (e) symmetric Hebbian rule, (f) symmetric *anti*-Hebbian rule. Reproduced with Permission [180]. Copyright 2016, Wiley-VCH.

transition from STM to LTM relies on the frequency of spikes [163]. In the synaptic transistor based on an $CsPbBr_3$ quantum dots, the drain current can be modulated by applied light pulses and decay to its initial state over time. This corresponds to STM, which is analogous to the human memory forgetting curve [183,184]. However, for repeated pulses, the altered drain current can persist longer. In addition, the improved stability and long-term retention can be realized by using different pulse parameters such as intensity, width, and number of repetitions.

For the $CsPbBr_3$ QDs/IGZO phototransistor in Ref. [160], electrical perturbation results in STP/LTD, while optical perturbation results in LTP. A combination of both electrical and optical programming pulses is applied in the classical conditioning experiments (Pavlov's dog) to demonstrate associative learning, an important tool for linking two events, i.e., a weak stimulus can be strengthened when it is concurrently associated with a strong stimulus.

In Ref. [37], John et al. reported $MAPbBr_3$, $FAPbBr_3$, and $CsPbBr_3$ based synaptic devices with demonstrated Hebbian STDP variants. A $4 \times 4$ $MAPbBr_3$-based synapse array was experimentally implemented. As in Fig. 18(a), the synapses are initially in stage i of the low-conductance state. The image of "N" is then written into the array by biasing (5 V, 10 s) selected individual pixels. With time lapsing (stage ii-iv), the conductance mapping via readout (+0.5 V, 1 s) still retains "N" but with reduced conductance contrast, in analogy to forgetting. On the other hand, "memory" can be completely recovered with shorter retraining pulses. Fig. 18(b) shows that "N" can be erased, and the array is reprogrammed into "T" or "U". The memory has good fault tolerance to spurious input, as demonstrated in Fig. 18(c). Thus, the HP-based synapses are demonstrated with properties of reconfigurability, learning, forgetting, and fault tolerance, like the human brain.

Based on the STDP behavior of $MAPbBr_3$ synapses, simulation was conducted for a 2-layer SNN to test its capability of unsupervised learning of handwritten digit selected from the MNIST database (Fig. 18(d)). All input pixels connect to each excitatory neuron in layer 1 through STDP synapses which are initialized with random weights. Each excitatory neuron connects to an inhibitory neuron in layer 2 through fixed weight synapses, introducing winner-take-all based competition among layer 1 neurons. Receptive field of neurons in the first layer resembles the handwritten digits after presentation of 6000 images in a randomized order through unsupervised learning with an accuracy of 80.8%. For learning, the HP approach has the potential to exhibit a significant reduction in energy over CMOS-based STDP implementations.

### 5.3. *Artificial sensory applications*

Sensory adaptation is an essential part of biological neural systems for sustaining human life. Leveraging the light-induced halide phase segregation and their slow recovery. Hong et al. reported $CsPb(Br_{1-x}I_x)_3/MoS_2$ hybrid structure based neuromorphic

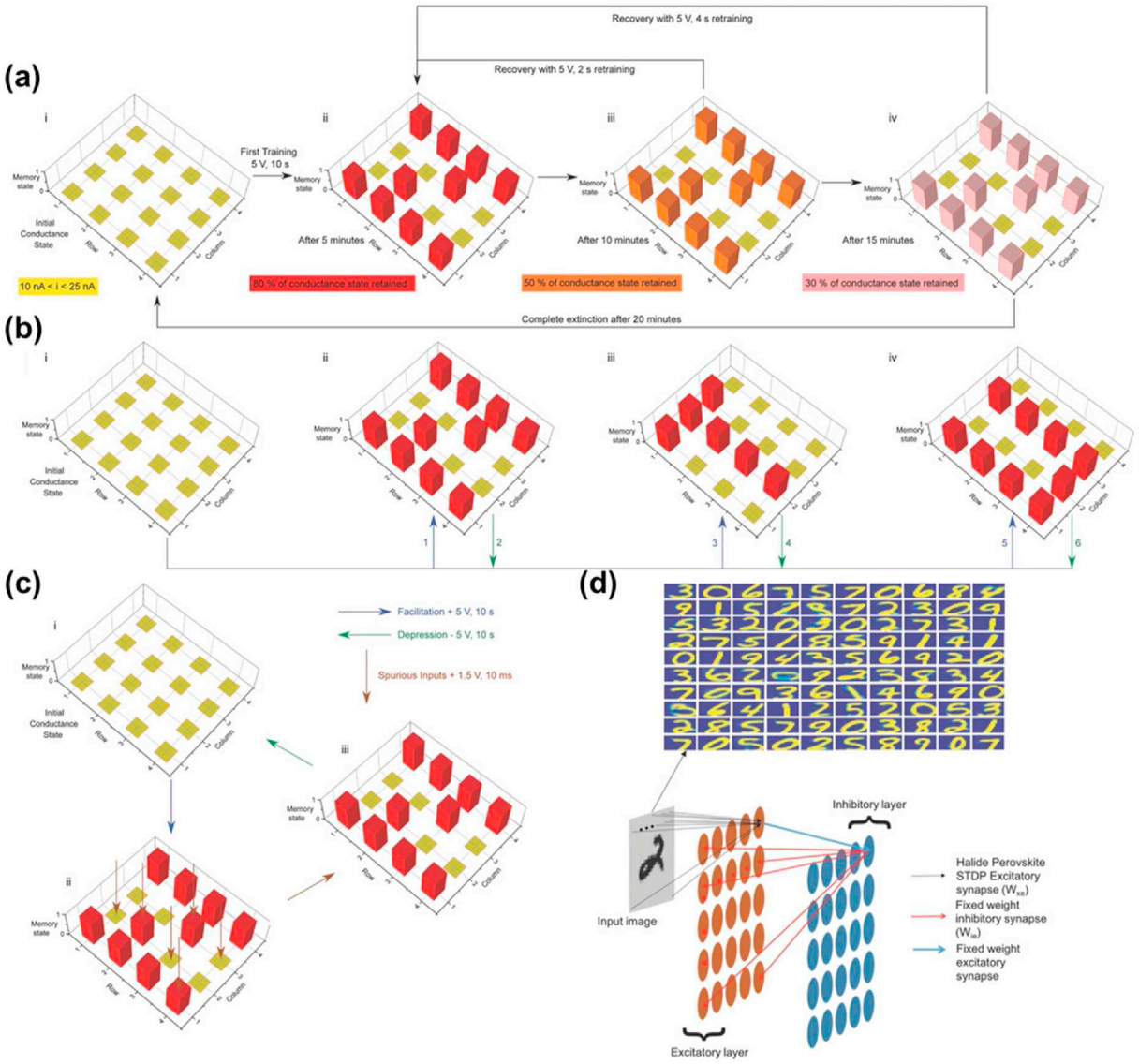


**Fig. 18.** (a) Schematic of 4 × 4 array of HP synapses. The image of "N" was programmed into the array using an external microcontroller biasing (5 V, 10 s) individual pixels on demand with others in a floating mode. With time, these synapses exhibited extinction of memory analogous to forgetting but could be retrained faster to reach the same conductance levels. (b) After complete erasing of the image of "N", "T" and "U" were also programmed and erased. (c) The memory array exhibits good fault tolerance and robustness to spurious inputs. (d) Schematic of two-layer SNN that is trained in simulations to recognize handwritten digits. The receptive fields of 100 neurons in the excitatory layer obtained after training on 6000 images are shown. Reproduced with Permission [37], copyright 2018 WILEY-VCH.

phototransistors that emulate human sensory adaptation in response to a continuous light stimulus (Fig. 19) [161]. Fig. 19(a) illustrates the eye anatomy, showing photoreceptors including cones and rods which convert light into electrical signals and transmit them to the brain. Fig. 19(b) compares the light adaption of human eye and the fabricated HP-based phototransistors. The underlying mechanism for the photo sensory adaptation is the segregation of halide ions in the mixed halide perovskites and their slow mixed phase recovery. For mixed-halide perovskites, the iodine-rich and bromine-rich domains can be induced by light stimulus, leading to the localized variations in the material band gap, which affects the separation of photo carriers at the interface between HP and $MoS_2$ semiconductor. After removing the stimuli, the segregated halide ions will start to slowly diffuse and recover their original mixed state, but this process takes time. Therefore, in this recovery period, photo response of the device on the next stimulus will be reduced, resulting in an adaption effect, similar to the memory of biological stimuli experience.

Fig. 19(c) shows variation of the photocurrents under constant light illumination as a function of time in four measurements. Each measurement lasts 60 s. Fig. 19(d) shows the time-resolved photoswitching characteristics of the phototransistor under pulsed light conditions. These data indicate that the HP-based phototransistor closely emulates the photosensory-adaptation behavior. The photosensitivity of the device emulating sensory adaptation is further shown in Fig. 19(e). The device characteristics are reversible upon the removal of the light stimulation, resulting in near-complete recovery of the photosensitivity before phase segregation occurs (96.65% sensitivity recovery after 5 min rest time). This type of phototransistor could be useful to other neuromorphic applications including neuromorphic photonic devices, intelligent sensors, and selective light-detecting image sensors.

As another approach to sensory applications, Guan et al. reported a $MAPbBr_3$-based monolithic artificial iconic memory,

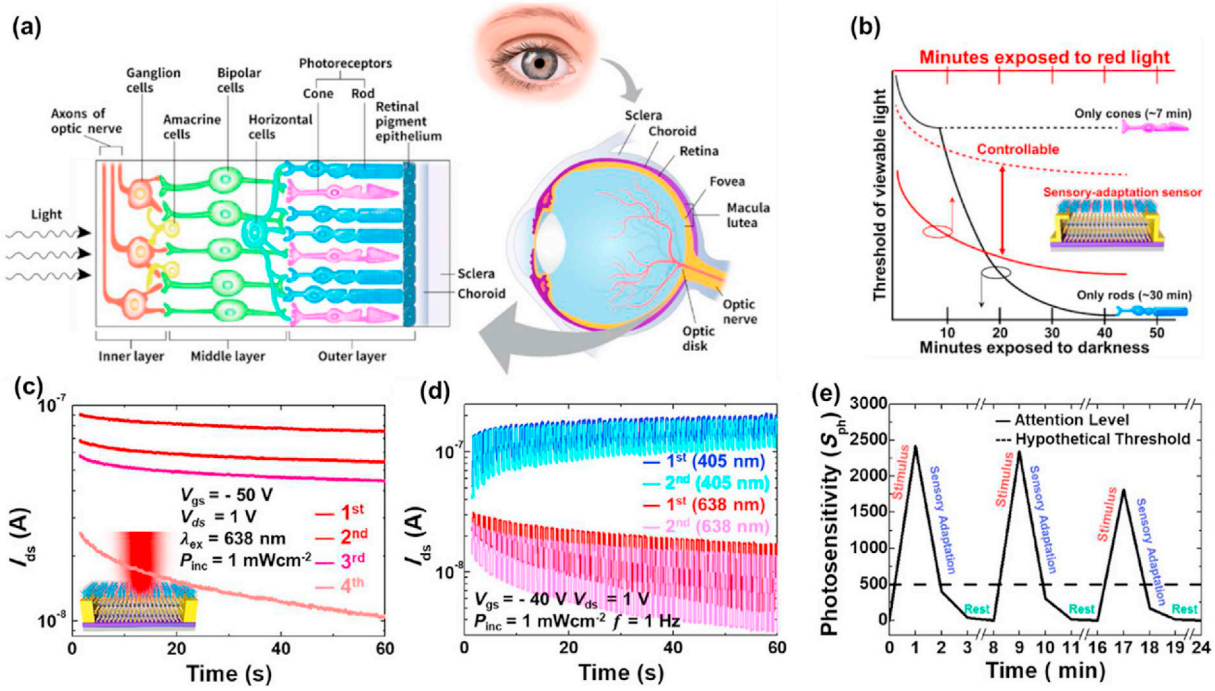


**Fig. 19.** Sensory adaptation of the eye and the $CsPb(Br_{0.5}I_{0.5})_3$–$MoS_2$ phototransistor. (a) Anatomy of the eye, with a photoreceptor comprising cones and rods. (b) Adaptation of the human eye and the $CsPb(Br_{0.5}I_{0.5})_3$–$MoS_2$ phototransistor. (c) Variation of the photocurrents under constant red-light illumination as a function of time in four measurements with each lasting 60 s. (d) Comparison of the time-resolved photo-switching characteristics of the phototransistor under pulsed light conditions. (e) Photosensitivity of the device emulating sensory adaptation. Reproduced with Permission [161], copyright 2020, American Chemical Society. (For interpretation of the references to colour in this figure legend, the reader is referred to the Web version of this article.)

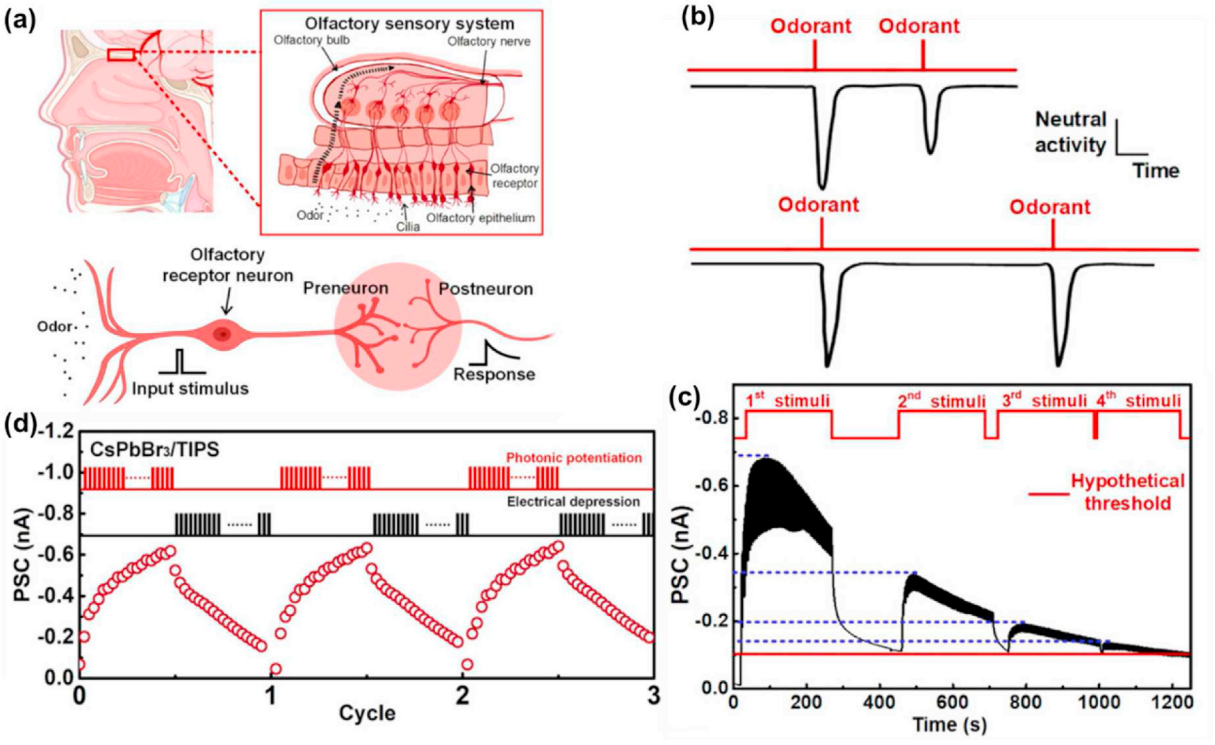


**Fig. 20.** (a) Schematic diagram of a human olfactory sensory system. (b) Adaptation of an intact olfactory receptor neuron. (c) A PSC example of the device with 50 sustained pulse stimuli separated by dark-rest periods emulating the olfactory adaptation. (d) Light potentiation and electrical depression of $CsPbBr_3$/TIPS hybrid device with three cycles. Reproduced with Permission [185], copyright 2021, American Chemical Society.

leveraging on the light-responsive and the RS properties of HP layers [169]. This multilayer perovskite device can store photosensing data in its resistive states, with a memory retention of 5 $\times$ $10^3$ s and presented excellent stability for 60 days in ambient conditions due to the stable RS characteristic. An array of such devices can detect and memorize spatial light intensity distribution.

A hybrid synaptic phototransistor based on the mixed-halide perovskite $CsPbBr_xI_{3-x}$/organic semiconductor TIPS film can mimic experience-history-dependent adaption sensory behavior [185]. Such devices also rely on photoinduced halide-ion segregation and their slow recovery properties. Fig. 20(a) illustrates how human olfactory system senses odorant molecules. When applying a 2nd odor stimulus in a short time after the 1st one, less neural activity is observed. The adaption of an intact olfactory receptor neuron is presented in Fig. 20(b). The postsynaptic current (PSC) of the $CsPbBr_xI_{3-x}$/TIP hybrid synaptic phototransistor presents a similar behavior, as shown in Fig. 20(c). That figure shows the response to 50 continued light pulses applied to the device. After a short dark-rest period, a 2nd set of pulses is applied and its PSC maximum response is smaller than the first. To improve their adaptability and perceptibility in different environments, varying the gate bias and the light pulse width, intensity, and wavelength can be done to further regulate the adaptation processes. On the other hand, if electrical depression is applied after light potentiation, as shown in Fig. 20(d), the maximum of PSC from each cycle exhibits only small fluctuation, thus preventing the sensory adaption. Owing to the excellent photosensitivity, this hybrid synaptic device can maintain its synaptic behavior for $V_{ds}$ as low as $-0.1$ mV with an extremely low power consumption of 0.35 fJ.

## 6. Summary comments

In this paper, we reviewed HP materials, their artificial synaptic devices, and preliminary demonstration of these devices in neuromorphic systems for information processing, including hardware-based implementation of DNNs and SNNs, as well as for sensory related applications.

### 6.1. Materials

The $ABX_3$ halide perovskite compounds and alloys share several desirable characteristics, including a low activation energy for ion diffusion, and controllable rates for ion migration, vacancy generation and charge carrier trapping and de-trapping. This facilitates the manipulation of both ions and electrons, in the tuning of conductivity, a highly advantageous property to produce HP-based synaptic devices. Importantly, by altering the composition via proper selection of A-site cations, B-site metal cations and X-site halide ions, the material's electronic, optical and defect properties, as well as the 2D or 3D structures, can be tailored. Their low material formation energies and soft structures render the possibility of engineering abundant “metastable” states. Solution-based facile material synthesis and relatively easy of integration with other materials, in particular with Si CMOS chips, are some other merits of this material system.

Their optical properties including their tunable bandgap, high absorption coefficient, and long charge carrier lifetimes, facilitating their use in the optical, in addition to the electrical mode. Photoinduced phase segregation in mixed halides provides further tools in states manipulating for better neuromorphic device design.

### 6.2. Devices

We focused on reviewing the mechanisms and operation characteristics of HP-based synaptic devices. The resistive switching behaviors in HP memristors stem from formation of metallic or vacancy-related filaments or the modulated Schottky junction between the electrode and the HP material. The capacitance changes in memcapacitors, induced by ion migration, offer the possibility to emulate the biological synapse. More interestingly, the synaptic weight in HP-based synaptic phototransistors can be modulated in a wide dynamic range due to their high photosensitivity, and small energy consumption. In fact, the energy dissipated when a combination of electrical and optical stimuli is used compares favorably to that of biological synapses (1–100 fJ/spike), Such HP-based artificial synapses exhibit synaptic plasticity including EPSC/IPSC, PPF, STP/LTP, STDP and memory transition characteristics.

Although HP-based synaptic devices have not yet met the industry-standard non-volatile memory requirement on retention and durance, these devices have relative low energy consumption compared to the more popular transition metal dichalcogenides (TMD) [187], phase change materials [188], and metal oxides [189] based synaptic devices. Table 2 illustrates several key synaptic performance metrics with HP-based memristors and synaptic transistors.

### 6.3. Systems

As proof of concepts, these neuromorphic devices were further included into neuromorphic systems, via simulation or preliminary experiments, to validate their performance at the system level. In DNNs, small and large MINST handwritten digits, as well as the more advanced Fashion MNIST standards have been used to demonstrate the high accuracy of the HP devices based ANNs in pattern recognition after off-line training. Similarly, HP devices that directly emulate biological neuron system have also been tested for learning and memorizing. Hebbian rules based STDP and associative learning, Atkinson and Shiffrin's memory retention model, and others have been established. Based on the STDP behavior of HP synapses, unsupervised learning of handwritten digits in an SNN was also simulated with reasonable accuracy and very high energy efficiency. HP-based hybrid neuromorphic phototransistors have also been applied to emulate human sensory adaptation in response to a continuous light stimulus and olfactory adaption.

The research on HP-based neuromorphic devices has mostly been focused on their application as synapses. It is interesting to note that a recent study reported that HP was applied for artificial neurons. Volatile diffusive $MAPbI_3$-based memristors with superior amplitude-frequency characteristics and highly linear conductivity modulation were employed to construct LIF neurons, which can implement leakage, spatiotemporal integration and firing functions [190]. More work is needed to be done in this area.

### 6.4. Challenges and opportunities

Despite the many inherent advantages and potentials of HP neuromorphic devices, there are still enormous challenges for them to be included in practical neuromorphic systems.

As has been clear, the soft nature of HPs, which results in low activation energy for ion diffusion and vacancy generation, low crystal formation energy that permit external stimuli-driven phase separation and restoration, among others, has played crucial roles in the HP's neuromorphic functions such as synaptic weight change, associative learning, memory retention, and sensory adaption. However, this soft nature is a double sword. A balance must be struck between easier adaption (meta-stable, or instable in some sense, particularly under extreme conditions) and long-term memory (stability).

The most significant challenge faced by HP-based synaptic

**Table 2**
Synaptic performance metrics for HP-based devices.

| Device type | Synapse type | Active layer | Energy consumption | Presynaptic spike width | PPF Index (A2/A1) | *STDP or SRDP* | Ref. |
|---|---|---|---|---|---|---|---|
| Memristor | Electrical mode | $MAPbBr_3$ | 34 fJ/μm$^2$ | 10 m s | 192 | Y | [37] |
| | | $FAPbBr_3$ | 23 fJ/μm$^2$ | | 145 | | |
| | | $CsPbBr_3$ | 153 fJ/μm$^2$ | | 104 | | |
| | | $MAPbBr_3$ | 20 fJ/spike | 100 m s | 90 | Y | [178] |
| | | $MAPbBr_3$ | 14.3 fJ/spike | 906 m s | 155 | | [186] |
| | | $(PEA)_2PbBr_4$ | 0.0003 fJ/μm$^2$ | 20 m s | 120 | Y | [58] |
| | | $MA_3Sb_2Br_9$ | 118 fJ/μm$^2$ | 500 μs | – | Y | [43] |
| | | $MAPbI_3$ | 0.003 fJ/μm$^2$ | 100 μs | – | Y | [180] |
| | | $MAPbI_3$ | 47 fJ/μm$^2$ | 100 μs | – | Y | [44] |
| | | $PEA_2Ma_{n-1}Pb_nI_{3n+1}$ | 60 nJ/spike | 10 m s | 135 | | [173] |
| | | $MAPbClBr_2$ | 5.8 pJ/spike | 25 m s | – | | [179] |
| | Photonic mode | $MAPbI_3$ | 0.0036 fJ/μm$^2$ | 0.4 s | – | | [171] |
| | Electrical/Photonic mode | $CsPbBr_3$ | – | 100 m s | 325 | | [177] |
| Transistor | Photonic mode | $CsPbBr_3$ | – | 500 m s | 132 | | [163] |
| | | $MAPbBr_3$ | 36.75 fJ/spike | 5 s | 160 | | [165] |
| | | $CsPbBr_3$ | 500 fJ/spike | 50 m s | 140 | Y | [160] |
| | | $CsPbBr_3$ | 1400 fJ/spike | 1 s | 130 | Y | [36] |
| | Electrical/Photonic mode | $CsPbBr_xI_{3-x}$ | 0.35 fJ/spike | 500 m s | 150 | | [185] |

devices perhaps is related to their material instability. Their sensitivity to heat and water vapor, particularly those inorganic-organic hybrids, leads to poor electrical and chemical stability, significant performance variability, and unsatisfied memory retention and endurance in many, if not all, demonstrations. Even though the instability of HPs is one of crucial issues that hinders their practical adoption, there are only a limited number of studies focused on improving the stability and durability of their synaptic devices [173,191]. Much more work is needed to enhance their stability under hardware running environmental conditions. The potential to exploit the relative stable 2D HPs, as well as engineering the HP device structures with interfacial layers between HP active layers and electrodes to control interdiffusion are appealing tactics. The method of using quantum dot passivation of HP films to suppress phase segregation and enhance stability is interesting [192]. The enormous efforts in developing stable HP photovoltaics certainly will also help the investigation in stable HP neuromorphic devices.

On the other hand, it is unclear at this stage whether HP-based synaptic nonvolatile memory ultimately could meet industry requirement of information retention for tens of years at ~85 °C and long cycle durance. These are the key requirements for synapses in DNNs, which rely more on deterministic computation and emphasize accuracy. In these systems, after time-consuming offline training, the synaptic weights should be permanently frozen into the NVM for the whole life cycle of the application. The scenario could be different in brain-plausible systems with real-time learning capability, where the stored synaptic weights are frequently refreshed and updated, and hence the stringent retention requirement might be largely loosed. However, devices must endure more cycles of update for continuous learning.

In this sense, research on HP neuromorphic devices perhaps should not be on their function as long-term memory but emphasizing more on their other functions. For instances, in many of the reported hybrid phototransistors, HPs are employed as the photosensitizer with other materials as the transistor channel. Since dynamics, at both the neuron and the network levels, are key property of brain-plausible systems, it would be much interesting to explore the potential of HPs for these functions, including for artificial neurons.

Considering that biological neural systems are composed of various components/materials with each playing its specific roles, it is reasonable to hypothesize that the future brain-plausible system also has a hybrid structure with materials heterogeneously integrating on a platform, in which, each component implements its optimized function. In such a hybrid artificial intelligent system, it is expected that halide perovskites, with their dynamic properties, electronic and ionic conductivities, photosensitivity, low energy consumption, and easily heterogeneous integration, could play some crucial roles.

## Declaration of competing interest

The authors declare that they have no known competing financial interests or personal relationships that could have appeared to influence the work reported in this paper.

## References


[1] A. Sebastian, M. Le Gallo, R. Khaddam-Aljameh, E. Eleftheriou, Memory devices and applications for in-memory computing, Nat. Nanotechnol. 15 (2020) 529–544.
[2] C.D. Schuman, T.E. Potok, R.M. Patton, J.D. Birdwell, M.E. Dean, G.S. Rose, J.S. Plank, A Survey of Neuromorphic Computing and Neural Networks in Hardware, 2017 *arXiv preprint arXiv:1705.06963*.
[3] D. Kuzum, S. Yu, H.P. Wong, Synaptic electronics: materials, devices and applications, Nanotechnology 24 (2013) 382001.
[4] G. Indiveri, S.-C. Liu, Memory and information processing in neuromorphic systems, Proc. IEEE 103 (2015) 1379–1397.
[5] V. Sze, Y.-H. Chen, T.-J. Yang, J.S. Emer, Efficient processing of deep neural networks: a tutorial and survey, Proc. IEEE 105 (2017) 2295–2329.
[6] A. Tavanaei, M. Ghodrati, S.R. Kheradpisheh, T. Masquelier, A. Maida, Deep learning in spiking neural networks, Neural Network. 111 (2019) 47–63.
[7] A. Cangelosi, S. Invitto, Human-Robot Interaction and Neuroprosthetics: a review of new technologies, IEEE Consumer Electronics Magazine 6 (2017) 24–33.
[8] A. Basu, J. Acharya, T. Karnik, H. Liu, H. Li, J.-S. Seo, C. Song, Low-power, adaptive neuromorphic systems: recent progress and future directions, IEEE Journal on Emerging and Selected Topics in Circuits and Systems 8 (2018) 6–27.
[9] J. Tang, D. Bishop, S. Kim, M. Copel, T. Gokmen, T. Todorov, S. Shin, K.-T. Lee, P. Solomon, K. Chan, ECRAM as scalable synaptic cell for high-speed, low-power neuromorphic computing, in: Proceedings of the 2018 IEEE International Electron Devices Meeting (IEDM), 2018, 13.11. 11-13.11. 14.
[10] M.T. Sharbati, Y. Du, J. Torres, N.D. Ardolino, M. Yun, F. Xiong, Low-power, electrochemically tunable graphene synapses for neuromorphic computing, Adv. Mater. 30 (2018) 1802353.
[11] V. Milo, C. Zambelli, P. Olivo, E. Pérez, K. Mahadevaiahm, G. Ossorioo, C. Wenger, D. Ielmini, Multilevel HfO2-based RRAM devices for low-power neuromorphic networks, Apl. Mater. 7 (2019): 081120.
[12] G. Wu, P. Feng, X. Wan, L. Zhu, Y. Shi, Q. Wan, Artificial synaptic devices based on natural chicken albumen coupled electric-double-layer transistors, Sci. Rep. 6 (2016) 1–9.
[13] Q. Wan, M.T. Sharbati, J.R. Erickson, Y. Du, F. Xiong, Emerging artificial synaptic devices for neuromorphic computing, Advanced Materials Technologies 4 (2019) 1900037.
[14] H.J. Kim, H. Zheng, J.-S. Park, D.H. Kim, C.J. Kang, J.T. Jang, D.H. Kim, T.-

S. Yoon, Artificial synaptic characteristics with strong analog memristive switching in a Pt/CeO2/Pt structure, Nanotechnology 28 (2017) 285203.
[15] G.W. Burr, R.M. Shelby, A. Sebastian, S. Kim, S. Kim, S. Sidler, K. Virwani, M. Ishii, P. Narayanan, A. Fumarola, Neuromorphic computing using non-volatile memory, Adv. Phys. X 2 (2017) 89–124.
[16] M.-K. Kim, Y. Park, I.-J. Kim, J.-S. Lee, Emerging materials for neuromorphic devices and systems, iScience (2020) 101846.
[17] M.K. Kim, J.S. Lee, Synergistic improvement of long-term plasticity in photonic synapses using ferroelectric polarization in hafnia-based oxide-semiconductor transistors, Adv. Mater. 32 (2020) 1907826.
[18] C.S. Yang, D.S. Shang, N. Liu, G. Shi, X. Shen, R.C. Yu, Y.Q. Li, Y. Sun, A synaptic transistor based on quasi-2D molybdenum oxide, Adv. Mater. 29 (2017) 1700906.
[19] J. Kim, Y. Kim, O. Kwon, T. Kim, S. Oh, S. Jin, W. Park, J.D. Kwon, S.W. Hong, C.S. Lee, Modulation of synaptic plasticity mimicked in Al nanoparticle-embedded IGZO synaptic transistor, Advanced Electronic Materials 6 (2020) 1901072.
[20] Z.-D. Luo, X. Xia, M.-M. Yang, N.R. Wilson, A. Gruverman, M. Alexe, Artificial optoelectronic synapses based on ferroelectric field-effect enabled 2D transition metal dichalcogenide memristive transistors, ACS Nano 14 (2019) 746–754.
[21] W. Huh, D. Lee, C.H. Lee, Memristors based on 2D materials as an artificial synapse for neuromorphic electronics, Adv. Mater. 32 (2020) 2002092.
[22] C. Zheng, Y. Liao, S.T. Han, Y. Zhou, Interface modification in three-terminal organic memory and synaptic device, Advanced Electronic Materials 6 (2020) 2000641.
[23] G.-T. Go, Y. Lee, D.-G. Seo, M. Pei, W. Lee, H. Yang, T.-W. Lee, Achieving microstructure-controlled synaptic plasticity and long-term retention in ion-gel-gated organic synaptic transistors, Advanced Intelligent Systems 2 (2020) 2000012.
[24] N.-G. Park, Perovskite solar cells: an emerging photovoltaic technology, Mater. Today 18 (2015) 65–72.
[25] P. Qin, S. Tanaka, S. Ito, N. Tetreault, K. Manabe, H. Nishino, M.K. Nazeeruddin, M. Grätzel, Inorganic hole conductor-based lead halide perovskite solar cells with 12.4% conversion efficiency, Nat. Commun. 5 (2014) 1–6.
[26] M. Ahmadi, T. Wu, B. Hu, A review on organic–inorganic halide perovskite photodetectors: device engineering and fundamental physics, Adv. Mater. 29 (2017) 1605242.
[27] J. Xing, F. Yan, Y. Zhao, S. Chen, H. Yu, Q. Zhang, R. Zeng, H.V. Demir, X. Sun, A. Huan, High-efficiency light-emitting diodes of organometal halide perovskite amorphous nanoparticles, ACS Nano 10 (2016) 6623–6630.
[28] A.K. Jena, A. Kulkarni, T. Miyasaka, Halide perovskite photovoltaics: background, status, and future prospects, Chem. Rev. 119 (2019) 3036–3103.
[29] K. Domanski, J.-P. Correa-Baena, N. Mine, M.K. Nazeeruddin, A. Abate, M. Saliba, W. Tress, A. Hagfeldt, M. Gratzel, Not all that glitters is gold: metal-migration-induced degradation in perovskite solar cells, ACS Nano 10 (2016) 6306–6314.
[30] A. Guerrero, J. You, C. Aranda, Y.S. Kang, G. Garcia-Belmonte, H. Zhou, J. Bisquert, Y. Yang, Interfacial degradation of planar lead halide perovskite solar cells, ACS Nano 10 (2016) 218–224.
[31] T. Zhang, X. Meng, Y. Bai, S. Xiao, C. Hu, Y. Yang, H. Chen, S. Yang, Profiling the organic cation-dependent degradation of organolead halide perovskite solar cells, J. Mater. Chem. 5 (2017) 1103–1111.
[32] D. Ielmini, G. Pedretti, Device and circuit architectures for in-memory computing, Advanced Intelligent Systems 2 (2020) 2000040.
[33] W. Zhang, B. Gao, J. Tang, P. Yao, S. Yu, M.-F. Chang, H.-J. Yoo, H. Qian, H. Wu, Neuro-inspired computing chips, Nature electronics 3 (2020) 371–382.
[34] S. Yu, Neuro-inspired computing with emerging nonvolatile memorys, Proc. IEEE 106 (2018) 260–285.
[35] J. del Valle, J.G. Ramírez, M.J. Rozenberg, I.K. Schuller, Challenges in materials and devices for resistive-switching-based neuromorphic computing, J. Appl. Phys. 124 (2018) 211101.
[36] Y. Wang, Z. Lv, J. Chen, Z. Wang, Y. Zhou, L. Zhou, X. Chen, S.T. Han, Photonic synapses based on inorganic perovskite quantum dots for neuromorphic computing, Adv. Mater. 30 (2018) 1802883.
[37] R.A. John, N. Yantara, Y.F. Ng, G. Narasimman, E. Mosconi, D. Meggiolaro, M.R. Kulkarni, P.K. Gopalakrishnan, C.A. Nguyen, F. De Angelis, Ionotronic halide perovskite drift-diffusive synapses for low-power neuromorphic computation, Adv. Mater. 30 (2018) 1805454.
[38] G. Perea, M. Navarrete, A. Araque, Tripartite synapses: astrocytes process and control synaptic information, Trends Neurosci. 32 (2009) 421–431.
[39] Y. Li, Y. Zhong, J. Zhang, L. Xu, Q. Wang, H. Sun, H. Tong, X. Cheng, X. Miao, Activity-dependent synaptic plasticity of a chalcogenide electronic synapse for neuromorphic systems, Sci. Rep. 4 (2014) 1–7.
[40] D.E. Feldman, The spike-timing dependence of plasticity, Neuron 75 (2012) 556–571.
[41] S. Song, K.D. Miller, L.F. Abbott, Competitive Hebbian learning through spike-timing-dependent synaptic plasticity, Nat. Neurosci. 3 (2000) 919–926.
[42] L.N. Cooper, M.F. Bear, The BCM theory of synapse modification at 30: interaction of theory with experiment, Nat. Rev. Neurosci. 13 (2012) 798–810.
[43] J.-M. Yang, E.-S. Choi, S.-Y. Kim, J.-H. Kim, J.-H. Park, N.-G. Park, Perovskite-related (CH 3 NH 3) 3 Sb 2 Br 9 for forming-free memristor and low-energy-consuming neuromorphic computing, Nanoscale 11 (2019) 6453–6461.
[44] B. Ku, B. Koo, A.S. Sokolov, M.J. Ko, C. Choi, Two-terminal artificial synapse with hybrid organic–inorganic perovskite (CH3NH3) PbI3 and low operating power energy (~ 47 fJ/μm2), J. Alloys Compd. 833 (2020) 155064.
[45] S. Yu, Y. Wu, R. Jeyasingh, D. Kuzum, H.-S.P. Wong, An electronic synapse device based on metal oxide resistive switching memory for neuromorphic computation, IEEE Trans. Electron. Dev. 58 (2011) 2729–2737.
[46] G. Pedretti, V. Milo, S. Ambrogio, R. Carboni, S. Bianchi, A. Calderoni, N. Ramaswamy, A. Spinelli, D. Ielmini, Memristive neural network for on-line learning and tracking with brain-inspired spike timing dependent plasticity, Sci. Rep. 7 (2017) 1–10.
[47] S. Kim, C. Du, P. Sheridan, W. Ma, S. Choi, W.D. Lu, Experimental demonstration of a second-order memristor and its ability to biorealistically implement synaptic plasticity, Nano Lett. 15 (2015) 2203–2211.
[48] Z. Wang, S. Joshi, S.E. Savel'ev, H. Jiang, R. Midya, P. Lin, M. Hu, N. Ge, J.P. Strachan, Z. Li, Memristors with diffusive dynamics as synaptic emulators for neuromorphic computing, Nat. Mater. 16 (2017) 101–108.
[49] B. Saparov, D.B. Mitzi, Organic–inorganic perovskites: structural versatility for functional materials design, Chem. Rev. 116 (2016) 4558–4596.
[50] J.-P. Correa-Baena, M. Saliba, T. Buonassisi, M. Grätzel, A. Abate, W. Tress, A. Hagfeldt, Promises and challenges of perovskite solar cells, Science 358 (2017) 739–744.
[51] G. Kieslich, S. Sun, A.K. Cheetham, Solid-state principles applied to organic–inorganic perovskites: new tricks for an old dog, Chem. Sci. 5 (2014) 4712–4715.
[52] G. Grancini, M.K. Nazeeruddin, Dimensional tailoring of hybrid perovskites for photovoltaics, Nat. Rev. Mater. 4 (2019) 4–22.
[53] S. Tao, I. Schmidt, G. Brocks, J. Jiang, I. Tranca, K. Meerholz, S. Olthof, Absolute energy level positions in tin-and lead-based halide perovskites, Nat. Commun. 10 (2019) 1–10.
[54] M.V. Kovalenko, L. Protesescu, M.I. Bodnarchuk, Properties and potential optoelectronic applications of lead halide perovskite nanocrystals, Science 358 (2017) 745–750.
[55] D.H. Cao, C.C. Stoumpos, O.K. Farha, J.T. Hupp, M.G. Kanatzidis, 2D homologous perovskites as light-absorbing materials for solar cell applications, J. Am. Chem. Soc. 137 (2015) 7843–7850.
[56] Y. Chen, Y. Sun, J. Peng, J. Tang, K. Zheng, Z. Liang, 2D Ruddlesden–Popper perovskites for optoelectronics, Adv. Mater. 30 (2018) 1703487.
[57] K. Tanaka, T. Kondo, Bandgap and exciton binding energies in lead-iodide-based natural quantum-well crystals, Sci. Technol. Adv. Mater. 4 (2003) 599–604.
[58] S.I. Kim, Y. Lee, M.H. Park, G.T. Go, Y.H. Kim, W. Xu, H.D. Lee, H. Kim, D.G. Seo, W. Lee, Dimensionality dependent plasticity in halide perovskite artificial synapses for neuromorphic computing, Advanced Electronic Materials 5 (2019) 1900008.
[59] S.M. Qaid, M.S. Al Sobaie, M.M. Khan, I.M. Bedja, F.H. Alharbi, M.K. Nazeeruddin, A.S. Aldwayyan, Band-gap tuning of lead halide perovskite using a single step spin-coating deposition process, Mater. Lett. 164 (2016) 498–501.
[60] S.A. Kulkarni, T. Baikie, P.P. Boix, N. Yantara, N. Mathews, S. Mhaisalkar, Band-gap tuning of lead halide perovskites using a sequential deposition process, J. Mater. Chem. 2 (2014) 9221–9225.
[61] Q. Ou, X. Bao, Y. Zhang, H. Shao, G. Xing, X. Li, L. Shao, Q. Bao, Band structure engineering in metal halide perovskite nanostructures for optoelectronic applications, Nano Materials Science 1 (2019) 268–287.
[62] R.F. Berger, Design principles for the atomic and electronic structure of halide perovskite photovoltaic materials: insights from computation, Chemistry–A European Journal 24 (2018) 8708–8716.
[63] M. Pandey, K.W. Jacobsen, K.S. Thygesen, Band gap tuning and defect tolerance of atomically thin two-dimensional organic–inorganic halide perovskites, J. Phys. Chem. Lett. 7 (2016) 4346–4352.
[64] O. Weber, B. Charles, M. Weller, Phase behaviour and composition in the formamidinium–methylammonium hybrid lead iodide perovskite solid solution, J. Mater. Chem. 4 (2016) 15375–15382.
[65] L. Lanzetta, J.M. Marin-Beloqui, I. Sanchez-Molina, D. Ding, S.A. Haque, Two-dimensional organic tin halide perovskites with tunable visible emission and their use in light-emitting devices, ACS Energy Lett. 2 (2017) 1662–1668.
[66] Y. Fang, Q. Dong, Y. Shao, Y. Yuan, J. Huang, Highly narrowband perovskite single-crystal photodetectors enabled by surface-charge recombination, Nat. Photonics 9 (2015) 679–686.
[67] T. Zhang, M. Yang, E.E. Benson, Z. Li, J. van de Lagemaat, J.M. Luther, Y. Yan, K. Zhu, Y. Zhao, A facile solvothermal growth of single crystal mixed halide perovskite CH 3 NH 3 Pb (Br 1− x Cl x) 3, Chem. Commun. 51 (2015) 7820–7823.
[68] K.X. Steirer, P. Schulz, G. Teeter, V. Stevanovic, M. Yang, K. Zhu, J.J. Berry, Defect tolerance in methylammonium lead triiodide perovskite, ACS Energy Lett. 1 (2016) 360–366.
[69] R.E. Brandt, J.R. Poindexter, P. Gorai, R.C. Kurchin, R.L. Hoye, L. Nienhaus, M.W. Wilson, J.A. Polizzotti, R. Sereika, R. Zaltauskas, Searching for "defect-tolerant" photovoltaic materials: combined theoretical and experimental screening, Chem. Mater. 29 (2017) 4667–4674.
[70] A. Buin, P. Pietsch, J. Xu, O. Voznyy, A.H. Ip, R. Comin, E.H. Sargent, Materials processing routes to trap-free halide perovskites, Nano Lett. 14 (2014) 6281–6286.
[71] W.-J. Yin, T. Shi, Y. Yan, Unusual defect physics in CH3NH3PbI3 perovskite solar cell absorber, Appl. Phys. Lett. 104 (2014): 063903.

[72] W. Ming, S. Chen, M.-H. Du, Chemical instability leads to unusual chemical-potential-independent defect formation and diffusion in perovskite solar cell material CH 3 NH 3 PbI 3, J. Mater. Chem. 4 (2016) 16975–16981.
[73] J. Kim, S.-H. Lee, J.H. Lee, K.-H. Hong, The role of intrinsic defects in methylammonium lead iodide perovskite, J. Phys. Chem. Lett. 5 (2014) 1312–1317.
[74] Q. Wang, Y. Shao, H. Xie, L. Lyu, X. Liu, Y. Gao, J. Huang, Qualifying composition dependent p and n self-doping in CH3NH3PbI3, Appl. Phys. Lett. 105 (2014) 163508.
[75] T. Shi, W.-J. Yin, F. Hong, K. Zhu, Y. Yan, Unipolar self-doping behavior in perovskite CH3NH3PbBr3, Appl. Phys. Lett. 106 (2015) 103902.
[76] H. Xie, X. Liu, L. Lyu, D. Niu, Q. Wang, J. Huang, Y. Gao, Effects of precursor ratios and annealing on electronic structure and surface composition of CH3NH3PbI3 perovskite films, J. Phys. Chem. C 120 (2016) 215–220.
[77] G. Paul, S. Chatterjee, H. Bhunia, A.J. Pal, Self-Doping in hybrid halide perovskites via precursor stoichiometry: to probe the type of conductivity through scanning tunneling spectroscopy, J. Phys. Chem. C 122 (2018) 20194–20199.
[78] Q. Chen, H. Zhou, Z. Hong, S. Luo, H.-S. Duan, H.-H. Wang, Y. Liu, G. Li, Y. Yang, Planar heterojunction perovskite solar cells via vapor-assisted solution process, J. Am. Chem. Soc. 136 (2014) 622–625.
[79] C. Bi, Y. Shao, Y. Yuan, Z. Xiao, C. Wang, Y. Gao, J. Huang, Understanding the formation and evolution of interdiffusion grown organolead halide perovskite thin films by thermal annealing, J. Mater. Chem. 2 (2014) 18508–18514.
[80] G. Cao, C. Cheng, H. Zhang, H. Zhang, R. Chen, B. Huang, X. Yan, W. Pei, H. Chen, The application of halide perovskites in memristors, J. Semiconduct. 41 (2020): 051205.
[81] M. Cherry, M.S. Islam, C. Catlow, Oxygen ion migration in perovskite-type oxides, J. Solid State Chem. 118 (1995) 125–132.
[82] H. Hayashi, H. Inaba, M. Matsuyama, N. Lan, M. Dokiya, H. Tagawa, Structural consideration on the ionic conductivity of perovskite-type oxides, Solid State Ionics 122 (1999) 1–15.
[83] M. Khan, M. Islam, D. Bates, Dopant substitution and ion migration in the LaGaO3-based oxygen ion conductor, J. Phys. Chem. B 102 (1998) 3099–3104.
[84] R.A. De Souza, M.S. Islam, E. Ivers-Tiffée, Formation and migration of cation defects in the perovskite oxide LaMnO 3, J. Mater. Chem. 9 (1999) 1621–1627.
[85] M.S. Islam, Ionic transport in ABO3 perovskite oxides: a computer modelling tour, J. Mater. Chem. 10 (2000) 1027–1038.
[86] M.N.F. Hoque, N. Islam, Z. Li, G. Ren, K. Zhu, Z. Fan, Ionic and optical properties of methylammonium lead iodide perovskite across the tetragonal–cubic structural phase transition, ChemSusChem 9 (2016) 2692–2698.
[87] H.J. Snaith, A. Abate, J.M. Ball, G.E. Eperon, T. Leijtens, N.K. Noel, S.D. Stranks, J.T.-W. Wang, K. Wojciechowski, W. Zhang, Anomalous hysteresis in perovskite solar cells, J. Phys. Chem. Lett. 5 (2014) 1511–1515.
[88] E.L. Unger, E.T. Hoke, C.D. Bailie, W.H. Nguyen, A.R. Bowring, T. Heumüller, M.G. Christoforo, M.D. McGehee, Hysteresis and transient behavior in current–voltage measurements of hybrid-perovskite absorber solar cells, Energy Environ. Sci. 7 (2014) 3690–3698.
[89] I. Zarazua, J. Bisquert, G. Garcia-Belmonte, Light-induced space-charge accumulation zone as photovoltaic mechanism in perovskite solar cells, J. Phys. Chem. Lett. 7 (2016) 525–528.
[90] E.J. Juarez-Perez, R.S. Sanchez, L. Badia, G. Garcia-Belmonte, Y.S. Kang, I. Mora-Sero, J. Bisquert, Photoinduced giant dielectric constant in lead halide perovskite solar cells, J. Phys. Chem. Lett. 5 (2014) 2390–2394.
[91] J. Mizusaki, K. Arai, K. Fueki, Ionic conduction of the perovskite-type halides, Solid State Ionics 11 (1983) 203–211.
[92] Y. Yuan, J. Huang, Ion migration in organometal trihalide perovskite and its impact on photovoltaic efficiency and stability, Acc. Chem. Res. 49 (2016) 286–293.
[93] D.A. Egger, L. Kronik, A.M. Rappe, Theory of hydrogen migration in organic–inorganic halide perovskites, Angew. Chem. Int. Ed. 54 (2015) 12437–12441.
[94] C. Eames, J.M. Frost, P.R. Barnes, B.C. O'regan, A. Walsh, M.S. Islam, Ionic transport in hybrid lead iodide perovskite solar cells, Nat. Commun. 6 (2015) 1–8.
[95] J.M. Azpiroz, E. Mosconi, J. Bisquert, F. De Angelis, Defect migration in methylammonium lead iodide and its role in perovskite solar cell operation, Energy Environ. Sci. 8 (2015) 2118–2127.
[96] J. Haruyama, K. Sodeyama, L. Han, Y. Tateyama, First-principles study of ion diffusion in perovskite solar cell sensitizers, J. Am. Chem. Soc. 137 (2015) 10048–10051.
[97] L. McGovern, M.H. Futscher, L.A. Muscarella, B. Ehrler, Understanding the stability of MAPbBr3 versus MAPbI3: suppression of methylammonium migration and reduction of halide migration, J. Phys. Chem. Lett. 11 (2020) 7127–7132.
[98] S.D. Stranks, V.M. Burlakov, T. Leijtens, J.M. Ball, A. Goriely, H.J. Snaith, Recombination kinetics in organic-inorganic perovskites: excitons, free charge, and subgap states, Physical Review Applied 2 (2014): 034007.
[99] D. Meggiolaro, E. Mosconi, F. De Angelis, Formation of surface defects dominates ion migration in lead-halide perovskites, ACS Energy Lett. 4 (2019) 779–785.
[100] W. Peng, B. Anand, L. Liu, S. Sampat, B.E. Bearden, A.V. Malko, Y.J. Chabal, Influence of growth temperature on bulk and surface defects in hybrid lead halide perovskite films, Nanoscale 8 (2016) 1627–1634.
[101] B. Conings, J. Drijkoningen, N. Gauquelin, A. Babayigit, J. D'Haen, L. D'Olieslaeger, A. Ethirajan, J. Verbeeck, J. Manca, E. Mosconi, Intrinsic thermal instability of methylammonium lead trihalide perovskite, Adv. Energy Mater. 5 (2015) 1500477.
[102] N. Phung, A. Al-Ashouri, S. Meloni, A. Mattoni, S. Albrecht, E.L. Unger, A. Merdasa, A. Abate, The role of grain boundaries on ionic defect migration in metal halide perovskites, Adv. Energy Mater. 10 (2020) 1903735.
[103] J.-S. Park, J. Calbo, Y.-K. Jung, L.D. Whalley, A. Walsh, Accumulation of deep traps at grain boundaries in halide perovskites, ACS Energy Lett. 4 (2019) 1321–1327.
[104] A.F. Castro-Méndez, J. Hidalgo, J.P. Correa-Baena, The role of grain boundaries in perovskite solar cells, Adv. Energy Mater. 9 (2019) 1901489.
[105] J.S. Yun, J. Seidel, J. Kim, A.M. Soufiani, S. Huang, J. Lau, N.J. Jeon, S.I. Seok, M.A. Green, A. Ho-Baillie, Critical role of grain boundaries for ion migration in formamidinium and methylammonium lead halide perovskite solar cells, Adv. Energy Mater. 6 (2016) 1600330.
[106] Y. Shao, Y. Fang, T. Li, Q. Wang, Q. Dong, Y. Deng, Y. Yuan, H. Wei, M. Wang, A. Gruverman, Grain boundary dominated ion migration in polycrystalline organic–inorganic halide perovskite films, Energy Environ. Sci. 9 (2016) 1752–1759.
[107] M.N.F. Hoque, R. He, J. Warzywoda, Z. Fan, Effects of moisture-based grain boundary passivation on cell performance and ionic migration in organic–inorganic halide perovskite solar cells, ACS Appl. Mater. Interfaces 10 (2018) 30322–30329.
[108] T. Zhang, C. Hu, S. Yang, Ion migration: a "double-edged sword" for halide-perovskite-based electronic devices, Small Methods 4 (2020) 1900552.
[109] M. Lai, A. Obliger, D. Lu, C.S. Kley, C.G. Bischak, Q. Kong, T. Lei, L. Dou, N.S. Ginsberg, D.T. Limmer, Intrinsic anion diffusivity in lead halide perovskites is facilitated by a soft lattice, Proc. Natl. Acad. Sci. Unit. States Am. 115 (2018) 11929–11934.
[110] J.F. Galisteo-López, Y. Li, H. Míguez, Three-dimensional optical tomography and correlated elemental analysis of hybrid perovskite microstructures: an insight into defect-related lattice distortion and photoinduced ion migration, J. Phys. Chem. Lett. 7 (2016) 5227–5234.
[111] Z. Xiao, Y. Yuan, Y. Shao, Q. Wang, Q. Dong, C. Bi, P. Sharma, A. Gruverman, J. Huang, Giant switchable photovoltaic effect in organometal trihalide perovskite devices, Nat. Mater. 14 (2015) 193–198.
[112] Y. Zhao, C. Liang, H. Zhang, D. Li, D. Tian, G. Li, X. Jing, W. Zhang, W. Xiao, Q. Liu, Anomalously large interface charge in polarity-switchable photovoltaic devices: an indication of mobile ions in organic–inorganic halide perovskites, Energy Environ. Sci. 8 (2015) 1256–1260.
[113] Y. Yuan, J. Chae, Y. Shao, Q. Wang, Z. Xiao, A. Centrone, J. Huang, Photovoltaic switching mechanism in lateral structure hybrid perovskite solar cells, Adv. Energy Mater. 5 (2015) 1500615.
[114] Y. Deng, Z. Xiao, J. Huang, Light-induced self-poling effect on organometal trihalide perovskite solar cells for increased device efficiency and stability, Adv. Energy Mater. 5 (2015) 1500721.
[115] E.T. Hoke, D.J. Slotcavage, E.R. Dohner, A.R. Bowring, H.I. Karunadasa, M.D. McGehee, Reversible photo-induced trap formation in mixed-halide hybrid perovskites for photovoltaics, Chem. Sci. 6 (2015) 613–617.
[116] D.J. Slotcavage, H.I. Karunadasa, M.D. McGehee, Light-induced phase segregation in halide-perovskite absorbers, ACS Energy Lett. 1 (2016) 1199–1205.
[117] L. Hu, X. Guan, W. Chen, Y. Yao, T. Wan, C.-H. Lin, N.D. Pham, L. Yuan, X. Geng, F. Wang, Linking phase segregation and photovoltaic performance of mixed-halide perovskite films through grain size engineering, ACS Energy Lett. 6 (2021) 1649–1658.
[118] S. Draguta, O. Sharia, S.J. Yoon, M.C. Brennan, Y.V. Morozov, J.S. Manser, P.V. Kamat, W.F. Schneider, M. Kuno, Rationalizing the light-induced phase separation of mixed halide organic–inorganic perovskites, Nat. Commun. 8 (2017) 1–8.
[119] L. Chua, Memristor-the missing circuit element, IEEE Trans. Circ. Theor. 18 (1971) 507–519.
[120] D.B. Strukov, G.S. Snider, D.R. Stewart, R.S. Williams, The missing memristor found, Nature 453 (2008) 80–83.
[121] J.R. Jameson, P. Blanchard, J. Dinh, N. Gonzales, V. Gopalakrishnan, B. Guichet, S. Hollmer, S. Hsu, G. Intrater, D. Kamalanathan, Conductive bridging RAM (CBRAM): then, now, and tomorrow, ECS Transactions 75 (2016) 41.
[122] D. Kim, S. Seo, S. Ahn, D.-S. Suh, M. Lee, B.-H. Park, I. Yoo, I. Baek, H.-J. Kim, E. Yim, Electrical observations of filamentary conductions for the resistive memory switching in NiO films, Appl. Phys. Lett. 88 (2006) 202102.
[123] Y. Wang, K.-M. Kang, M. Kim, H.-S. Lee, R. Waser, D. Wouters, R. Dittmann, J.J. Yang, H.-H. Park, Mott-transition-based RRAM, Mater. Today 28 (2019) 63–80.
[124] E.W. Lim, R. Ismail, Conduction mechanism of valence change resistive switching memory: a survey, Electronics 4 (2015) 586–613.
[125] F. Zeng, Y. Guo, W. Hu, Y. Tan, X. Zhang, J. Feng, X. Tang, Opportunity of the lead-free all-inorganic Cs3Cu2I5 perovskite film for memristor and neuromorphic computing applications, ACS Appl. Mater. Interfaces 12 (2020) 23094–23101.
[126] E. Yoo, M. Lyu, J.-H. Yun, C. Kang, Y. Choi, L. Wang, Bifunctional resistive switching behavior in an organolead halide perovskite based Ag/CH 3 NH 3 PbI 3− x Cl x/FTO structure, J. Mater. Chem. C 4 (2016) 7824–7830.

[127] J. Choi, S. Park, J. Lee, K. Hong, D.H. Kim, C.W. Moon, G.D. Park, J. Suh, J. Hwang, S.Y. Kim, Organolead halide perovskites for low operating voltage multilevel resistive switching, Adv. Mater. 28 (2016) 6562–6567.
[128] Y. Sun, M. Tai, C. Song, Z. Wang, J. Yin, F. Li, H. Wu, F. Zeng, H. Lin, F. Pan, Competition between metallic and vacancy defect conductive filaments in a CH3NH3PbI3-based memory device, J. Phys. Chem. C 122 (2018) 6431–6436.
[129] X. Zhao, H. Xu, Z. Wang, Y. Lin, Y. Liu, Memristors with organic-inorganic halide perovskites, Info 1 (2019) 183–210.
[130] C. Gu, J.-S. Lee, Flexible hybrid organic–inorganic perovskite memory, ACS Nano 10 (2016) 5413–5418.
[131] Y. Lin, F. Zeng, S. Tang, H. Liu, C. Chen, S. Gao, Y. Wang, F. Pan, Resistive switching mechanisms relating to oxygen vacancies migration in both interfaces in Ti/HfOx/Pt memory devices, J. Appl. Phys. 113 (2013): 064510.
[132] Y. Shuai, Y. Peng, X. Pan, L. Jin, C. Wu, W. Luo, H. Zeng, W. Zhang, Coexistence of memristive and memcapacitive effects in oxide thin films, Jpn. J. Appl. Phys. 57 (2018) 121502.
[133] W. Hu, N. Qin, G. Wu, Y. Lin, S. Li, D. Bao, Opportunity of spinel ferrite materials in nonvolatile memory device applications based on their resistive switching performances, J. Am. Chem. Soc. 134 (2012) 14658–14661.
[134] Y.C. Yang, F. Pan, Q. Liu, M. Liu, F. Zeng, Fully room-temperature-fabricated nonvolatile resistive memory for ultrafast and high-density memory application, Nano Lett. 9 (2009) 1636–1643.
[135] W. Hu, L. Zou, R. Chen, W. Xie, X. Chen, N. Qin, S. Li, G. Yang, D. Bao, Resistive switching properties and physical mechanism of cobalt ferrite thin films, Appl. Phys. Lett. 104 (2014) 143502.
[136] C. Chen, C. Song, J. Yang, F. Zeng, F. Pan, Oxygen migration induced resistive switching effect and its thermal stability in W/TaO x/Pt structure, Appl. Phys. Lett. 100 (2012) 253509.
[137] X. Guan, W. Hu, M.A. Haque, N. Wei, Z. Liu, A. Chen, T. Wu, Light-responsive ion-redistribution-induced resistive switching in hybrid perovskite Schottky junctions, Adv. Funct. Mater. 28 (2018) 1704665.
[138] J.S. Han, Q.V. Le, J. Choi, H. Kim, S.G. Kim, K. Hong, C.W. Moon, T.L. Kim, S.Y. Kim, H.W. Jang, Lead-free all-inorganic cesium tin iodide perovskite for filamentary and interface-type resistive switching toward environment-friendly and temperature-tolerant nonvolatile memories, ACS Appl. Mater. Interfaces 11 (2019) 8155–8163.
[139] F. Zhou, Y. Liu, X. Shen, M. Wang, F. Yuan, Y. Chai, Low-voltage, optoelectronic CH3NH3PbI3− xClx memory with integrated sensing and logic operations, Adv. Funct. Mater. 28 (2018) 1800080.
[140] H. Ma, W. Wang, H. Xu, Z. Wang, Y. Tao, P. Chen, W. Liu, X. Zhang, J. Ma, Y. Liu, Interface state-induced negative differential resistance observed in hybrid perovskite resistive switching memory, ACS Appl. Mater. Interfaces 10 (2018) 21755–21763.
[141] E.J. Yoo, M. Lyu, J.H. Yun, C.J. Kang, Y.J. Choi, L. Wang, Resistive switching behavior in organic–inorganic hybrid CH3NH3PbI3− xClx perovskite for resistive random access memory devices, Adv. Mater. 27 (2015) 6170–6175.
[142] M. Di Ventra, Y.V. Pershin, L.O. Chua, Circuit elements with memory: memristors, memcapacitors, and meminductors, Proc. IEEE 97 (2009) 1717–1724.
[143] R. Liu, R. Dong, X. Yan, S. Yuan, D. Zhang, B. Yang, X. Xiao, Two-parameter multi-state memory device based on memristance and memcapacitance characteristics, APEX 11 (2018) 114103.
[144] S. Goswami, S.P. Rath, D. Thompson, S. Hedström, M. Annamalai, R. Pramanick, B.R. Ilic, S. Sarkar, S. Hooda, C.A. Nijhuis, Charge disproportionate molecular redox for discrete memristive and memcapacitive switching, Nat. Nanotechnol. 15 (2020) 380–389.
[145] A. Daus, C. Roldán-Carmona, K. Domanski, S. Knobelspies, G. Cantarella, C. Vogt, M. Grätzel, M.K. Nazeeruddin, G. Tröster, Metal-halide perovskites for gate dielectrics in field-effect transistors and photodetectors enabled by PMMA lift-off process, Adv. Mater. 30 (2018) 1707412.
[146] O. Almora, I. Zarazua, E. Mas-Marza, I. Mora-Sero, J. Bisquert, G. Garcia-Belmonte, Capacitive dark currents, hysteresis, and electrode polarization in lead halide perovskite solar cells, J. Phys. Chem. Lett. 6 (2015) 1645–1652.
[147] I. Anusca, S. Balčiūnas, P. Gemeiner, Š. Svirskas, M. Sanlialp, G. Lackner, C. Fettkenhauer, J. Belovickis, V. Samulionis, M. Ivanov, Dielectric response: answer to many questions in the methylammonium lead halide solar cell absorbers, Adv. Energy Mater. 7 (2017) 1700600.
[148] T.Y. Yang, G. Gregori, N. Pellet, M. Grätzel, J. Maier, The significance of ion conduction in a hybrid organic–inorganic lead-iodide-based perovskite photosensitizer, Angew. Chem. Int. Ed. 54 (2015) 7905–7910.
[149] M.N.F. Hoque, M. Yang, Z. Li, N. Islam, X. Pan, K. Zhu, Z. Fan, Polarization and dielectric study of methylammonium lead iodide thin film to reveal its nonferroelectric nature under solar cell operating conditions, ACS Energy Lett. 1 (2016) 142–149.
[150] W.H. Qian, X.F. Cheng, Y.Y. Zhao, J. Zhou, J.H. He, H. Li, Q.F. Xu, N.J. Li, D.Y. Chen, J.M. Lu, Independent memcapacitive switching triggered by bromide ion migration for quaternary information storage, Adv. Mater. 31 (2019) 1806424.
[151] B. Li, R. Long, Y. Xia, Q. Mi, All-inorganic perovskite CsSnBr3 as a thermally stable, free-carrier semiconductor, Angew. Chem. Int. Ed. 57 (2018) 13154–13158.
[152] J.M. Frost, A. Walsh, What is moving in hybrid halide perovskite solar cells? Acc. Chem. Res. 49 (2016) 528–535.
[153] L. Zhao, Z. Fan, S. Cheng, L. Hong, Y. Li, G. Tian, D. Chen, Z. Hou, M. Qin, M. Zeng, An artificial optoelectronic synapse based on a photoelectric memcapacitor, Advanced Electronic Materials 6 (2020) 1900858.
[154] R. Liu, R. Dong, S. Qin, X. Yan, A new type artificial synapse based on the organic copolymer memcapacitor, Org. Electron. 81 (2020) 105680.
[155] S. Bhattacharjee, R. Wigchering, H.G. Manning, J.J. Boland, P.K. Hurley, Emulating synaptic response in n-and p-channel MoS 2 transistors by utilizing charge trapping dynamics, Sci. Rep. 10 (2020) 1–8.
[156] K. Beom, P. Yang, D. Park, H.J. Kim, H.H. Lee, C.J. Kang, T.-S. Yoon, Single-and double-gate synaptic transistor with TaOx gate insulator and IGZO channel layer, Nanotechnology 30 (2018): 025203.
[157] Y. Zang, H. Shen, D. Huang, C.A. Di, D. Zhu, A dual-organic-transistor-based tactile-perception system with signal-processing functionality, Adv. Mater. 29 (2017) 1606088.
[158] Q. Lai, L. Zhang, Z. Li, W.F. Stickle, R.S. Williams, Y. Chen, Ionic/electronic hybrid materials integrated in a synaptic transistor with signal processing and learning functions, Adv. Mater. 22 (2010) 2448–2453.
[159] C.S. Yang, D.S. Shang, N. Liu, E.J. Fuller, S. Agrawal, A.A. Talin, Y.Q. Li, B.G. Shen, Y. Sun, All-Solid-state synaptic transistor with ultralow conductance for neuromorphic computing, Adv. Funct. Mater. 28 (2018) 1804170.
[160] S. Subramanian Periyal, M. Jagadeeswararao, S.E. Ng, R.A. John, N. Mathews, Halide perovskite quantum dots photosensitized-amorphous oxide transistors for multimodal synapses, Advanced Materials Technologies 5 (2020) 2000514.
[161] S. Hong, S.H. Choi, J. Park, H. Yoo, J.Y. Oh, E. Hwang, D.H. Yoon, S. Kim, Sensory adaptation and neuromorphic phototransistors based on CsPb (Br1−x I x) 3 perovskite and MoS2 hybrid structure, ACS Nano 14 (2020) 9796–9806.
[162] D. Hao, J. Zhang, S. Dai, J. Zhang, J. Huang, Perovskite/organic semiconductor-based photonic synaptic transistor for artificial visual system, ACS Appl. Mater. Interfaces 12 (2020) 39487–39495.
[163] K. Wang, S. Dai, Y. Zhao, Y. Wang, C. Liu, J. Huang, Light-stimulated synaptic transistors fabricated by a facile solution process based on inorganic perovskite quantum dots and organic semiconductors, Small 15 (2019) 1900010.
[164] Y. Sun, L. Qian, D. Xie, Y. Lin, M. Sun, W. Li, L. Ding, T. Ren, T. Palacios, Photoelectric synaptic plasticity realized by 2D perovskite, Adv. Funct. Mater. 29 (2019) 1902538.
[165] B. Pradhan, S. Das, J. Li, F. Chowdhury, J. Cherusseri, D. Pandey, D. Dev, A. Krishnaprasad, E. Barrios, A. Towers, Ultrasensitive and ultrathin phototransistors and photonic synapses using perovskite quantum dots grown from graphene lattice, Sci. Adv. 6 (2020): eaay5225.
[166] F. Li, C. Ma, H. Wang, W. Hu, W. Yu, A.D. Sheikh, T. Wu, Ambipolar solution-processed hybrid perovskite phototransistors, Nat. Commun. 6 (2015) 1–8.
[167] Y. Zou, F. Li, C. Zhao, J. Xing, Z. Yu, W. Yu, C. Guo, Anomalous ambipolar phototransistors based on all-inorganic CsPbBr3 perovskite at room temperature, Adv. Opt. Mater. 7 (2019) 1900676.
[168] Y. Mei, C. Zhang, Z. Vardeny, O. Jurchescu, Electrostatic gating of hybrid halide perovskite field-effect transistors: balanced ambipolar transport at room-temperature, MRS Communications 5 (2015) 297–301.
[169] X. Guan, Y. Wang, C.-H. Lin, L. Hu, S. Ge, T. Wan, A. Younis, F. Li, Y. Cui, D.-C. Qi, A monolithic artificial iconic memory based on highly stable perovskite-metal multilayers, Appl. Phys. Rev. 7 (2020): 031401.
[170] X. Guan, T. Wan, L. Hu, C.H. Lin, J. Yang, J.K. Huang, C.Y. Huang, S. Shahrokhi, A. Younis, K. Ramadass, A solution-processed all-perovskite memory with dual-band light response and tri-mode operation, Adv. Funct. Mater. (2022) 2110975.
[171] S. Ham, S. Choi, H. Cho, S.I. Na, G. Wang, Photonic organolead halide perovskite artificial synapse capable of accelerated learning at low power inspired by dopamine-facilitated synaptic activity, Adv. Funct. Mater. 29 (2019) 1806646.
[172] Y. Park, M.-K. Kim, J.-S. Lee, 2D layered metal-halide perovskite/oxide semiconductor-based broadband optoelectronic synaptic transistors with long-term visual memory, J. Mater. Chem. C 9 (2021) 1429–1436.
[173] S.J. Kim, T.H. Lee, J.-M. Yang, J.W. Yang, Y.J. Lee, M.-J. Choi, S.A. Lee, J.M. Suh, K.J. Kwak, J.H. Baek, Vertically aligned two-dimensional halide perovskites for reliably operable artificial synapses, Mater. Today (2021), https://doi.org/10.1016/j.mattod.2021.10.035.
[174] R.S. Zucker, W.G. Regehr, Short-term synaptic plasticity, Annu. Rev. Physiol. 64 (2002) 355–405.
[175] L. Abbott, W.G. Regehr, Synaptic computation, Nature 431 (2004) 796–803.
[176] A.M. Thomson, Facilitation, augmentation and potentiation at central synapses, Trends Neurosci. 23 (2000) 305–312.
[177] F. Ma, Y. Zhu, Z. Xu, Y. Liu, X. Zheng, S. Ju, Q. Li, Z. Ni, H. Hu, Y. Chai, Optoelectronic perovskite synapses for neuromorphic computing, Adv. Funct. Mater. 30 (2020) 1908901.
[178] W. Xu, H. Cho, Y.H. Kim, Y.T. Kim, C. Wolf, C.G. Park, T.W. Lee, Organometal halide perovskite artificial synapses, Adv. Mater. 28 (2016) 5916–5922.
[179] H. Yu, J. Gong, H. Wei, W. Huang, W. Xu, Mixed-halide perovskite for ultrasensitive two-terminal artificial synaptic devices, Mater. Chem. Front. 3 (2019) 941–947.
[180] Z. Xiao, J. Huang, Energy-efficient hybrid perovskite memristors and synaptic devices, Advanced Electronic Materials 2 (2016) 1600100.
[181] L.F. Abbott, S.B. Nelson, Synaptic plasticity: taming the beast, Nat. Neurosci. 3 (2000) 1178–1183.
[182] R.M. Shiffrin, R.C. Atkinson, Storage and retrieval processes in long-term memory, Psychol. Rev. 76 (1969) 179.

[183] T. Chang, S.-H. Jo, W. Lu, Short-term memory to long-term memory transition in a nanoscale memristor, ACS Nano 5 (2011) 7669–7676.
[184] D.C. Rubin, S. Hinton, A. Wenzel, The precise time course of retention, J. Exp. Psychol. Learn. Mem. Cognit. 25 (1999) 1161.
[185] J. Liu, Z. Shen, Y. Ye, Z. Yang, Z. Gong, B. Ye, Y. Qiu, Q. Huang, L. Xu, Y. Zhou, Mixed-halide perovskite film-based neuromorphic phototransistors for mimicking experience-history-dependent sensory adaptation, ACS Appl. Mater. Interfaces 13 (2021) 47807–47816.
[186] J. Choi, Q.V. Le, K. Hong, C.W. Moon, J.S. Han, K.C. Kwon, P.-R. Cha, Y. Kwon, S.Y. Kim, H.W. Jang, Enhanced endurance organolead halide perovskite resistive switching memories operable under an extremely low bending radius, ACS Appl. Mater. Interfaces 9 (2017) 30764–30771.
[187] L. Sun, Y. Zhang, G. Hwang, J. Jiang, D. Kim, Y.A. Eshete, R. Zhao, H. Yang, Synaptic computation enabled by joule heating of single-layered semiconductors for sound localization, Nano Lett. 18 (2018) 3229–3234.
[188] D. Kuzum, R.G. Jeyasingh, B. Lee, H.-S.P. Wong, Nanoelectronic programmable synapses based on phase change materials for brain-inspired computing, Nano Lett. 12 (2012) 2179–2186.
[189] Y. Matveyev, K. Egorov, A. Markeev, A. Zenkevich, Resistive switching and synaptic properties of fully atomic layer deposition grown TiN/HfO2/TiN devices, J. Appl. Phys. 117 (2015): 044901.
[190] J.-Q. Yang, R. Wang, Z.-P. Wang, Q.-Y. Ma, J.-Y. Mao, Y. Ren, X. Yang, Y. Zhou, S.-T. Han, Leaky integrate-and-fire neurons based on perovskite memristor for spiking neural networks, Nano Energy 74 (2020) 104828.
[191] R. Wang, M. Mujahid, Y. Duan, Z.K. Wang, J. Xue, Y. Yang, A review of perovskites solar cell stability, Adv. Funct. Mater. 29 (2019) 1808843.
[192] L. Hu, L. Duan, Y. Yao, W. Chen, Z. Zhou, C. Cazorla, C.H. Lin, X. Guan, X. Geng, F. Wang, Quantum dot passivation of halide perovskite films with reduced defects, suppressed phase segregation, and enhanced stability, Adv. Sci. 9 (2022) 2102258.